JGR Space Physics

RESEARCH ARTICLE
10.1029/2022JA031069

Wavelike Oscillations in High Latitude Thermospheric Doppler Temperature and Line-Of-Sight Wind Observed Using All-Sky Imaging Fabry-Perot Spectrometers

R. Itani[1] **and M. Conde**[1]

[1]Geophysical Institute, University of Alaska Fairbanks, Fairbanks, AK, USA

Key Points:

- Thermospheric gravity wave (GW) signatures were derived by high-pass filtering winds and temperatures acquired using optical Doppler spectroscopy
- Wave activity was almost always seen in F-region winds with a strong correlation between magnetic activity and oscillation amplitudes
- Not all oscillations were due to traveling waves, however, those that were appeared consistent with previous GW observations

Supporting Information:

Supporting Information may be found in the online version of this article.

Correspondence to:

R. Itani,
ritani@alaska.edu

Citation:

Itani, R., & Conde, M. (2023). Wavelike oscillations in high latitude thermospheric Doppler temperature and line-of-sight wind observed using all-sky imaging Fabry-Perot spectrometers. *Journal of Geophysical Research: Space Physics*, *128*, e2022JA031069. https://doi.org/10.1029/2022JA031069

Received 17 OCT 2022
Accepted 29 AUG 2023

Abstract Multiple years of thermospheric wind and temperature data were examined to study gravity waves in Earth's thermosphere. Winds and temperatures were measured using all-sky imaging optical Doppler spectrometers deployed at two sites in Alaska, and three in Antarctica. For all sites, oscillatory perturbations were clearly present in high-pass temporally filtered F-region line-of-sight (LOS) winds for the majority of the clear-sky nights. Oscillations were also discernible in E-region LOS wind and F-region Doppler temperature, albeit less frequently. Oscillation amplitudes correlated strongly with auroral and geomagnetic activity. Observed wave signatures also correlated strongly between geographically nearby observing sites. Amplitudes of LOS wind oscillations were usually small when viewed in the zenith and increased approximately with the sine of the zenith angle—as expected if the underlying motion is predominantly horizontal. Scanning Doppler Imager instruments observe in many look directions simultaneously. Phase relationships between perturbations observed in different look directions were used to identify time intervals when the oscillations were likely to be due to traveling waves. However, a number of instances were noted in which the oscillations had characteristics suggesting geophysical mechanisms other than traveling waves—a recognition that was only possible because of the large number of look directions. Lomb-Scargle analysis was used on a representative subset of days to resolve the spectral distributions of the wind and temperature oscillations. F-region wind oscillations on days analyzed this way exhibited periods typically ranging from 60 min and above. By contrast, E-region wind oscillation periods were as short as 30 min.

Plain Language Summary Atmospheric neutral wind and temperature measurements from polar regions were analyzed from two different altitudes—~120 and ~240 km. Wavelike oscillations were a nearly ubiquitous feature of winds observed at 240 km altitude. Similar oscillations were also detected in temperatures at 240 km and in winds at 120 km, although these later oscillations were weaker than those of the upper region winds. These oscillations, if visualized, would appear as a complicated wave field manifesting various sizes and propagation directions, in a manner somewhat analogous to surface waves on the ocean. Amplitudes of these oscillations responded strongly to geomagnetic activity, with large waves occurring after the onset of strong magnetic perturbations and persisting for several hours. Our instruments sample more than a hundred look directions in the sky at once. This allows for higher confidence in extracting wave signatures than would be possible using data from just a single look direction.

1. Introduction

Earth's thermosphere is convectively stable and has a very high kinematic viscosity, which means that small-scale wind structures are not expected to form in the absence of strong and localized external forcing (e.g., Killeen et al., 1988; Killeen & Roble, 1988). Nevertheless, air parcels displaced vertically by local forcing would experience a restoring force due to an imbalance between buoyancy and gravity. This mechanism would allow so-called gravity waves (GWs) to propagate away from the disturbance. There is ample evidence that such waves are indeed commonly observed in the thermosphere (e.g., Djuth et al., 1997, 2004; England et al., 2020; Hocke & Schlegel, 1996; Oliver et al., 1997; Yiğit & Medvedev, 2012).

Thermospheric GWs can either be generated in situ or can result from dissipation and breaking of waves propagating upward from lower atmospheric layers (Fritts & Alexander, 2003; Vadas & Fritts, 2006). In-situ generation of GWs in the auroral zone is a common outcome of geomagnetic disturbances (Oyama et al., 2001). GWs generated by mechanisms involving local energy deposition in the thermosphere typically have large relative amplitudes compared to similar waves in the lower atmosphere and have wavelengths larger than 1,000 km (Garcia

et al., 2016). They are thus relatively easy to observe. Observations show that large-scale thermospheric GWs occur even during quiet geomagnetic conditions suggesting that such waves may have been excited from below (Bruinsma & Forbes, 2008; Vadas & Liu, 2009). All but the largest scale of waves propagating upwards from the lower atmosphere dissipate before reaching the thermosphere. Dissipation of upward propagating waves deposits energy and momentum into the background atmosphere, which generates a broad spectrum of secondary GWs, better suited to survive in the thermosphere (Vadas & Azeem, 2020). These secondary GWs exhibit horizontal scales that are much larger than those of the primary GWs (Vadas et al., 2018).

Itani and Conde (2021) investigated an abrupt stalling of the cross-polar jet in the midnight sector over Alaska. They reported that the characteristic length scale of the stalling could be as short as ∼200 km. Further, Innis (2000) has reported more gradual stalling of the cross-polar jet. Innis (2000) suggested that one of the possible mechanisms for the stalling of the cross-polar jet could be the dissipation of GWs. These observations suggest that GWs may play an important role in thermospheric dynamics. However, details of this role are not fully understood, partly because of the difficulty of observing these waves across an extended geographic region—which is one of the major motivations for the present study.

A number of techniques have been used for observing thermospheric GWs (England et al., 2020, and references therein). For example, waves cause brightness variations in monochromatic (narrow-band) images of upper atmospheric airglow recorded by all-sky cameras. Low Earth orbit satellites cannot observe temporal evolution at a fixed location because of their orbital motion. Nevertheless, spacecraft can monitor wave perturbations along the orbit at what is essentially an instantaneous time because, at an average orbital speed of ∼8 km/s, the time taken to move a distance comparable to the wave's horizontal wavelength is generally significantly less than the wave's temporal period. However, there is no guarantee that the orbital direction is parallel to the wave's horizontal k-vector, which means that orbiting spacecraft measure the horizontal trace wavelength rather than the intrinsic wavelength. Radio techniques such as ionosondes, radars, and total electron content measured by global navigation satellite system networks can also be used to detect GWs. These methods are sensitive to wave perturbations in ionospheric electron density. In addition to the perturbation by electric and magnetic fields, ion and electron number density and momentum fields are also perturbed by collisional coupling with neutral particles. Oscillatory perturbations in the neutral fields, such as wind, temperature etc., should thus be reflected in the coupled oscillatory perturbations in the ions and electrons. Conversely, ion and electron oscillations can drive an oscillation in the neutral fields. Waves observed through electron density fluctuations are typically referred to as traveling ionospheric disturbances.

The techniques discussed above provide measurements of a number of different atmospheric parameters. However, some of these parameters are more directly related to wave propagation than others. Temperature, wind, pressure, and mass density are the fluid fields involved in the dynamical response that allows waves to propagate. The existence and characteristics of GW oscillations can be observed via perturbations in these quantities. Alternatively, other indirect proxy fields may be observed to infer the existence and characteristics of thermospheric GWs. Common examples of wave detection via proxy fields would be through imaging airglow variations (Fukushima et al., 2012; Hickey et al., 2010; Paulino et al., 2016), or recording oscillatory changes in ionospheric electron density (Galvan et al., 2011). The distinction between primary and proxy fields is whether the perturbations are associated with the wave's restoring force and propagation mechanism. Proxy fields play no role in the wave propagation mechanism.

2. Instruments and Methods

2.1. Instrumentation

A common technique for ground-based remote sensing of thermospheric wind and temperature uses optical Doppler spectroscopy of airglow and/or auroral emissions. In this study, thermospheric winds and temperatures (and oscillatory perturbations to these quantities) were derived from Doppler shifts and Doppler broadening, measured using all-sky imaging Fabry-Perot spectrometer (FPS) instruments. FPSs have been used in several studies that have adopted this technique (e.g., Conde et al., 2001; Hays et al., 1969; Hernandez, 1982; Innis et al., 1996; Nicolls et al., 2012). However, until recently, the sensitivity of typical instruments provided limited ability to characterize the wave oscillations in the primary fields. The latest generations of FPSs now offer much-improved sensitivity. The particular implementation of the FPS technique used here is known as a Scanning

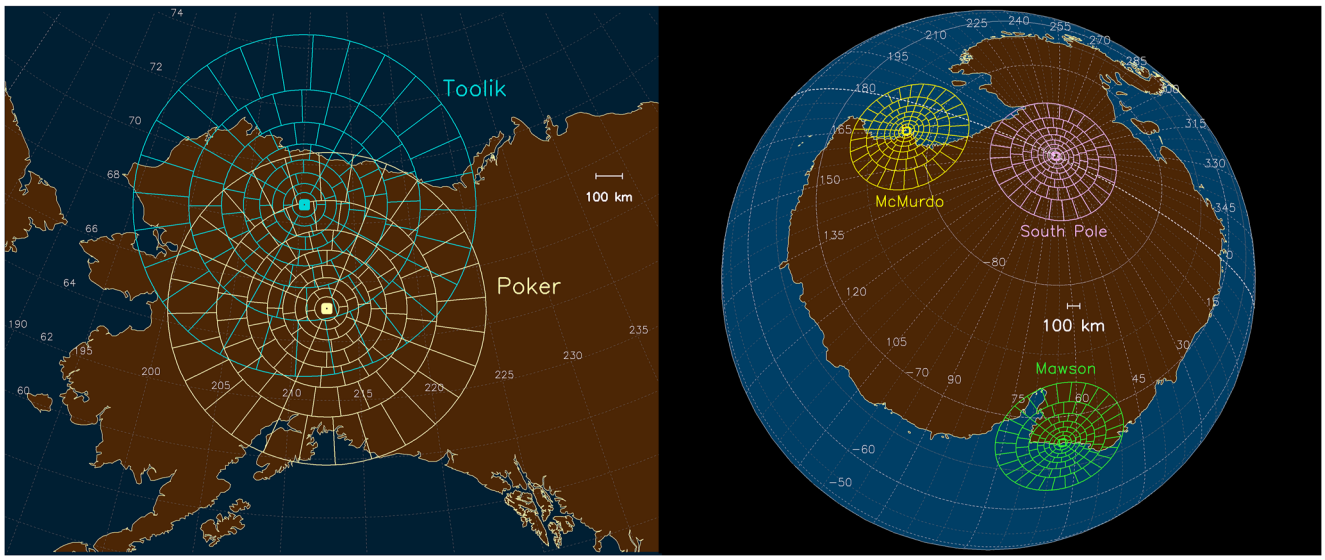

Figure 1. Field of view (FoV) projected at peak red-line emission altitudes for Scanning Doppler Imager instruments located at Toolik Lake and Poker Flat in Alaska (left panel), and Mawson, McMurdo, and South Pole stations in Antarctica (right panel). The two Alaskan instruments have significant overlap in their FoVs. However, the Antarctic stations are far apart from each other such that there is no overlap in the instrument's FoVs.

Doppler Imager (SDI), which exploits high sensitivity to provide the capability to look in many directions at once. This makes wave characterization much more tractable than before. Our group has been operating SDIs for more than 20 years. In this work, SDI data have been used to extract periodic perturbations in temperature and line-of-sight (LOS) wind. Further, data were examined from instruments in both the northern hemisphere (Alaska) and the southern hemisphere (Antarctica). To our knowledge, this is the first study to compare thermospheric wave activity in both hemispheres using passive optical Doppler spectroscopy.

The object-space SDI Field of view (FoV) in the sky can be configured to encompass any solid angle (up to 2π steradian). The typical configuration views a zenith-centered field that extends out to about 75° zenith angle. This FoV is subdivided (using image processing software) into many different contiguous sub-fields arranged in a set of concentric rings divided into sectors. The sub-fields are referred to as "zones," of which there are 115 in total for the standard configuration. Examples of the standard zone maps for instruments located at Poker Flat and Toolik Lake in Alaska and at Mawson, McMurdo and South Pole in Antarctica, projected onto an altitude of 240 km, are shown in Figure 1. There are several rings (typically seven) around the zenith, and each of the rings spans 360° in azimuth. There are more azimuthal sectors in the outer rings, so the solid angles subtended by all zones are approximately similar.

Table 1
Locations of the Five Different Scanning Doppler Imager Instruments Used in This Work

Station name	Geographic latitude	Geographic longitude	Geomagnetic latitude
Toolik Lake	68° 38′ N	149° 36′ W	68° 44′ N
Poker Flat	65° 07′ N	147° 29′ W	65° 31′ N
Mawson	67° 36′ S	62° 52′ E	70° 32′ S
McMurdo	77° 50′ S	166° 40′ E	79° 59′ S
South Pole	90° 00′ S	–	74° 18′ S

Note. Coordinates have been rounded to the nearest arc minute. Geomagnetic latitudes were obtained from the Virtual Ionosphere Thermosphere Mesosphere Observatory magnetic field model (https://omniweb.gsfc.nasa.gov/vitmo/cgm.html) for the year 2015.

Exposure times typically vary in the range of 2–10 min, depending on auroral activity and resulting emission brightness. Within any given exposure the SDI records the optical spectrum of the airglow/aurora for each zone, over a wavelength interval spanning approximately 10 p.m., with a spectral resolution of 1 p.m. or less. The sky spectrum is then fitted numerically to derive the Doppler temperature and LOS component of the wind associated with each zone. An example of the resulting data acquired by an SDI observing in its standard mode is depicted in Figure 1 of Conde et al. (2018).

SDI data from two Alaskan sites (Toolik Lake and Poker Flat) and three Antarctic sites (Mawson, McMurdo, and the South Pole) are shown in the current work. The geographic locations of these five sites are given in Table 1. SDIs provide useful diagnostics for studying thermospheric GWs because they measure the temperature and wind fields that are directly associated with the wave propagation in the thermosphere (i.e., they are not proxy fields). Furthermore, the all-sky imaging capability allows the construction of 2D-geographic maps of the perturbation fields.

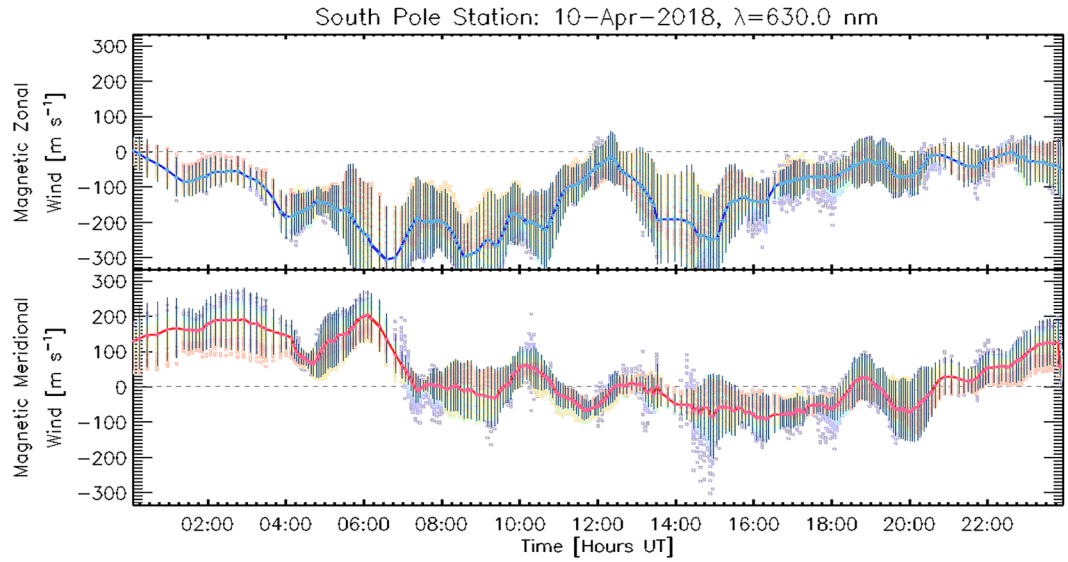

Figure 2. Wind summary plot derived from 630 nm spectra (originating from F-region heights) for the day of 10 April 2018, as observed from the Earth's geographic South Pole. The solid blue and red traces in the top and middle panels respectively show the median of the fitted magnetic zonal and magnetic meridional winds from all look directions at a given time. Individual dots in these panels are color-coded according to the look azimuths and represent the fitted wind in each zone. The rainbow-colored swaths around the traces are composed of a number of those dots, most of which are unresolved. A few of them are discernible away from the curves. Black vertical bars on top of the median wind traces show the standard deviation of observed wind speeds in all the zones at a given time. Note that geographic zonal and meridional directions are undefined at the pole. However, no such problem applies to the geomagnetic directions used here.

SDI instruments operate automatically and observe the sky whenever the solar depression angle exceeds 9° (which is required to allow the weak airglow or auroral emissions to be isolated from the background scattered sunlight). Unfortunately, the resulting data do contain periods when the measurements are not indicative of geophysical conditions in the thermosphere—for example, due to observing through the heavy tropospheric cloud or as a result of serious instrumental problems. The first step in data processing was to apply various quality controls to select only those periods when the measurements satisfied criteria for validity that we have established empirically over 25 years of operation of these instruments. Quality parameters include the signal-to-noise ratio for accumulated spectra, reduced chi-square of the spectral fitting, and the parameter estimates themselves. Further, a test that examines the Doppler shifts across the FoV and over time was used to recognize and eliminate cloudy days. For this study, automatically acquired SDI data were examined from sites at Toolik Lake (2012–2021), and Poker Flat (2009–2021) in Alaska and Mawson (2011–2014), McMurdo (2016–2019), and South Pole (2016–2018) in Antarctica. Note, we also examined data from another Alaskan site located near the town of Gakona. Although the behavior observed at Gakona was similar to that at other sites none of these data appear explicitly in this study. All together, a total of approximately 3,000 nights of independent observations were examined. The overall data set is too large to present here. Instead, we will simply show some representative examples of physically important characteristics that were commonly present in the data. Also, we will discuss some general behaviors that we observed when examining the larger data set.

2.2. The Routine Vector Wind Product

The standard analysis of SDI spectra produces estimates of the LOS component of the wind for each of the 115 look directions (Conde, 2001). Subsequent analysis, using procedures as described in Conde and Smith (1998), is then used to estimate zonal and meridional wind components for each zone at each time. Figure 2 shows examples of the time series of the medians of the F-region fitted vector wind components over all 115 look directions, observed from Earth's geographic South Pole on the night of 10 April 2018. The winds are resolved into magnetic zonal and meridional components using a Cartesian coordinate system in which the magnetic north direction is defined by the oval angle specified by the Virtual Ionosphere Thermosphere Mesosphere Observatory magnetic field model. Vertical bars in both panels of Figure 2 do not indicate wind uncertainties. Rather, they indicate the

standard deviation of values observed in the wind components across all the zones at each time. A larger vertical bar indicates greater wind variation across the FoV.

Although the fitted vector wind components are of most interest for understanding thermospheric dynamics at synoptic scales and larger, the fitting process generates vector components using all 115 zones together. However, the horizontal wavelengths of thermospheric GWs can be comparable to or smaller than the synoptic scale. A product derived from all look directions across the ∼1,000 km diameter FoV would suppress fluctuations that are local to one (or just a few) of the look directions. Further, as explained in detail by Anderson et al. (2012) and Conde and Smith (1998), vector fitting requires a number of significant assumptions. These assumptions are reasonable when applied over the whole FoV. However, they are almost certainly inappropriate for single-zone data. Overall, the fitted vector winds most likely would not capture wave oscillations very accurately. Therefore, for extraction of wave perturbations, it is far better to use the original LOS wind estimates, which are derived solely from the spectra observed in individual zones. Uncertainties in LOS wind estimates vary depending on the emission brightness. For example, as shown in Figure 8 of Itani and Conde (2021), the distribution of uncertainties when the emission brightness is weak has a Gaussian shape, peaking at ∼14 m/s. However, smaller uncertainties are obtained during bright aurora and are ∼5 m/s. These values span the typical range of LOS wind uncertainties.

2.3. Signal Processing: Extraction of Perturbations in Temperature and LOS Wind

A high-pass temporal filter was used to extract high-frequency oscillations in the observed temperatures and LOS winds. Wind and temperature perturbations were obtained, for each zone, as a function of time during the night. Filtering was done in the Fourier transform domain. The filter transmission was tuned to begin attenuating periods longer than 180 min. Transform coefficients for 180 min period were multiplied by 0.5. All remaining coefficients for periods longer than 180 min were multiplied by zero. Variations over time scales longer than this are likely to reflect the slowly varying forcing experienced by the thermosphere as a result of changing local time, and hence may not be indicative of traveling waves. Additionally, oscillation periods of 12 min or less for F-region and 7 min or less for E-region were suppressed in the current analysis to attenuate noise. Such filtering is unlikely to conceal any valid geophysical information because these times are comparable to the Brunt-Väisälä period at the respective altitudes (Yeh & Liu, 1974; Yu, 2007) (Strictly, this means our data were band-pass filtered although the salient property of the processing was to provide high-pass filtering.). Finally, the sampling cadence of SDI data is typically longer than 5 min except under active geomagnetic conditions. During active conditions, individual exposure times can be as short as 1 min. However, typical exposure times are longer—2 min or more. Further, the normal observing sequence includes alternate red-line and green-line observations, resulting in a typical data cadence of about 4–5 min. Because of this, the measurements are interpolated onto a regular time grid sampled at 1 min cadence, which is adequate even for the most rapid sampling cadence that the instrument can obtain.

Figure 3 presents an example of applying the high-pass filter to the 115 time series of LOS winds. In this format (which is also used for a number of subsequent figures) high-pass filtered signals from each zone are plotted with a small vertical displacement between successive traces to produce a stack plot. The ordering of traces in the stack is such that the traces near the bottom correspond to zones near the zenith, whereas those near the top represent zones near the horizon. The color assigned to each trace is based on the look azimuth of the corresponding zone, with the mapping of azimuth to color being implemented via a cyclic palette. This ensures that there is no color discontinuity after 360° of azimuthal rotation. Because there are more azimuthal sectors near the horizon than near the center, the color banding is more spread near the top of the wave plots.

Many days of SDI data from various stations have been examined in this study. Wavelike oscillatory wind and temperature perturbations appeared very commonly during clear-sky observations. To illustrate the types of behavior observed, 6 days of data that exhibited pronounced oscillatory perturbations have been chosen from the observational archive (As SDI instruments acquire data only during darkness, the word “day” should only be interpreted as referring to the date of observations.). Lomb-Scargle analysis was performed to find the typical periods associated with these waves.

As will be discussed in later sections, not all oscillatory perturbations seen in the data are indicative of propagating waves. The best way to unambiguously identify signatures of a propagating wave would be to reconstruct the

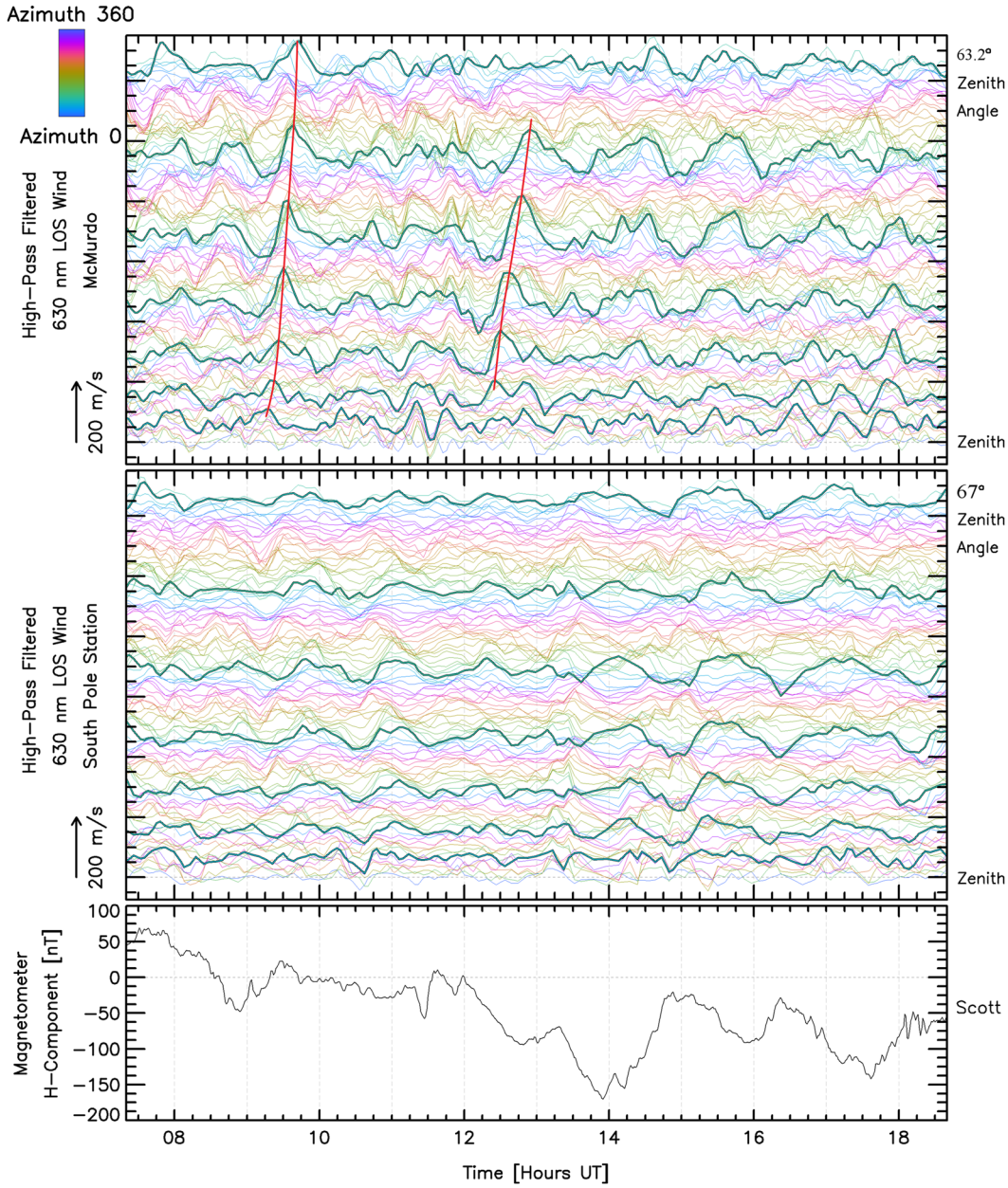

Figure 3. The top and middle panels show line-of-sight (LOS) wind oscillations observed from McMurdo and South Pole stations respectively, during the night of 10 April 2018. The magnitude of LOS wind oscillations is indicated by the scale arrow on the bottom left of each panel. The color bar on the top left shows the azimuthal directions of the zones to which the stacked wave plots correspond. Traces near the bottom of each of the top two panels correspond to zones near the zenith, whereas those toward the top represent zones near the horizon. Each field of view was divided into 115 zones, and hence there are 115 independent traces in each panel. Green colored thick traces highlight zones at similar azimuth (Highlighted azimuths are near 160° in the top panel and near 200° in the middle panel, and were chosen because the LOS component oscillations were strong in these directions.). The two red-colored free drawings in the top panel between 9 and 10 UT, and 12 and 13 UT are depicting the time lags between prominent example perturbations observed at different zenith angles but similar azimuth. The bottom panel shows the trace of the magnetometer H-component observed at Scott Base, Antarctica.

phase fronts and the propagation directions based on phase lags between the various look directions. However, such analysis is not straightforward and is beyond the scope of this initial survey. Rather, this preliminary study will instead merely flag examples in which perturbations across a large portion of the FoV manifest phase lags that appear qualitatively consistent with a propagating wave, and determine whether such events appear to be correlated with times of elevated geomagnetic activity.

3. Results

Oscillatory perturbations were recognizable (relative to measurement noise) in LOS winds in most of the data that passed the quality controls. In many cases, the oscillations were weak but unambiguously present. The strongest oscillatory perturbations typically corresponded to times of elevated magnetic activity. These general behaviors are illustrated by the following examples.

3.1. Wavelike Perturbations in Doppler Temperatures and LOS Wind Components

3.1.1. F-Region LOS Wind Oscillations

The top and middle panels in Figure 3 show wavelike oscillations in LOS winds recorded by SDI instruments located at McMurdo and the South Pole stations in Antarctica, during the same night as shown in Figure 2—that is, 10 April 2018. These wind oscillations were extracted from the LOS components of winds derived from 630.0 nm atomic oxygen spectra. The bottom panel shows the geomagnetic H-component recorded during this period at Scott Base, Antarctica, which is ∼3 km from McMurdo Station. Wave activity (as indicated by wave amplitudes) on this day was intermediate between the levels of activity observed on the quietest and most active days in our data set. Consistent with other examples presented here, this level of wave activity was commensurate with the moderately disturbed magnetic activity on this day as indicated by the lower panel of Figure 3 and three hourly Kp indices for the observation period which were 4, 3−, 3+, 3, and 2+. The solar radio flux index (F10.7) was 68.8 solar flux units (sfu), although there does not appear to be a strong correlation between F10.7 and wave activity within the data sets presented in this paper. Note that Figure 2 shows a large-scale background wind. This has been removed from all the stack plots presented in this paper by the high-pass filtering process.

McMurdo and South Pole instruments are independent, and these stations are geographically separated by a large distance (∼1,350 km), which means that their F-region fields of view do not overlap. Nevertheless, there is some indication that the most active period in the South Pole data also corresponded to the most active period at McMurdo. The amplitudes of perturbations in Figure 3 (and in subsequent LOS wind stack plots) are smallest for zones near the zenith and they increase gradually toward the outer zones closer to the horizon, as would be expected if the oscillations were primarily due to perturbations in the horizontal wind. Further, oscillations between adjacent zones are highly coherent. These characteristics strongly indicate an actual geophysical origin for the wave oscillations extracted from the observations. Note that the oscillations are not perfect sinusoids, illustrating that the perturbations are not strictly monochromatic.

Importantly, the data frequently showed time lags among the look azimuths. Time lags among the oscillations arising from different parts of the sky are conspicuous in the upper panel of Figure 3 between 12 and 13 UT. Another example of time lag in the LOS components of the wind can also be seen between 9 and 10 UT in the upper panel in Figure 3. In this figure, looking at the oscillations coming from similar azimuths (highlighted traces), the peak oscillations shift by ∼15 min for the traces near the top of the plot relative to the traces near the bottom. This behavior is as expected considering the previously observed propagation speeds (∼500 m/s) of storm time F-region wind oscillations (Johnson et al., 1995), and the ∼500 km radius of all-sky FoV of the SDI instrument at 240 km altitude.

On this night, oscillation amplitudes recorded at McMurdo were larger than those at South Pole. Caution should be taken that the high-pass filtered wind perturbation amplitudes vary not only because the elevation angle varies across the FoV, but also because the look azimuth varies across the FoV as well. In the later case, the amplitude varies according to the cosine of the angle between the horizontal oscillation direction and the look direction. It is quite difficult to fully resolve the contributions of these two effects for data presented in the stack plot format.

3.1.2. Simultaneous Oscillation Signatures in LOS Wind Data Captured by Nearby SDIs

There were many instances where SDI instruments with some overlap in their FoV simultaneously observed similar oscillatory features in their high-pass filtered LOS wind data. For example, the top and middle panels in Figure 4 respectively show wavelike perturbations in F-region LOS winds as observed from Toolik Lake and Poker Flat, Alaska on 14 October 2016. The bottom panel shows the H-component of the geomagnetic field perturbation, recorded at College, Alaska, which is ∼30 km southwest of Poker Flat. The two SDI observing sites are located ∼400 km apart and have some overlap (more than 60%) in their fields of view at ∼240 km altitude. Note that, at this altitude, each instrument's FoV is ∼1,000 km in diameter. The collection and analysis of data

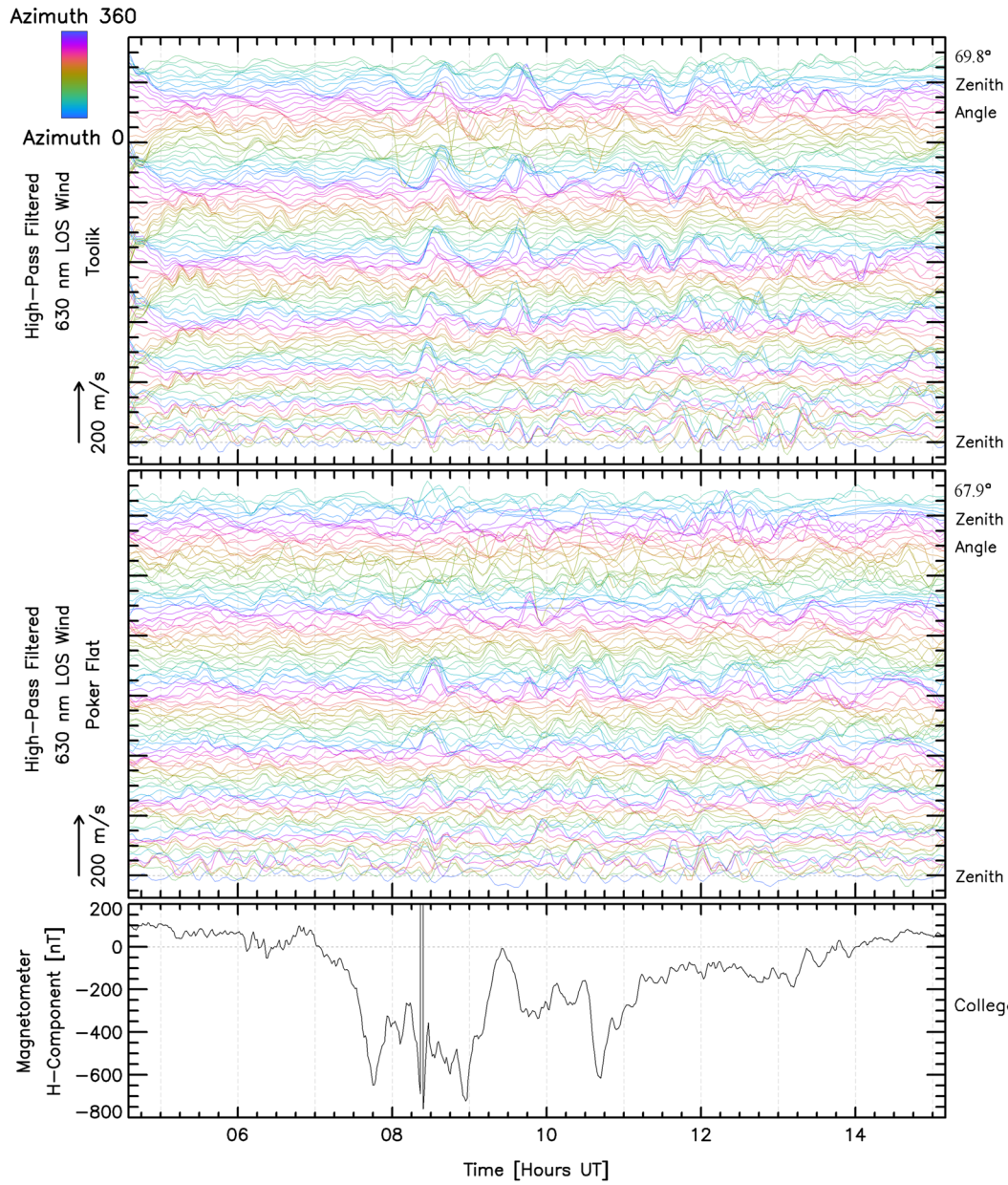

Figure 4. Same as Figure 3, but now showing measurements from Toolik Lake and Poker Flat, Alaska, for the night of 14 October 2016. The bottom panel depicts the H-component of the magnetic field perturbation recorded at College, Alaska. The spike in the magnetometer data between 8:15 and 8:30 UT in the bottom panel represents an artifact. On this day, the F10.7 index was 92.3 sfu, and three hourly Kp indices from 3 to 15 UT, which also span the observation period, were 5−, 5−, 3, and 2−.

from these two instruments are completely independent; there is no instrumental or data processing mechanism that could couple the results shown in the top two panels of Figure 4. Nevertheless, the time series of high-pass filtered LOS wind from each station show instances of very similar responses at times, which can only have occurred as a result of the two instruments observing the same geophysical oscillations. In particular, the onset of a similar burst of oscillations was observed at both sites at ∼8 UT. Relatively weak wind perturbations prevailed prior to this point. However, after this time, strong wavelike oscillations persisted for the rest of the night. Note that the dynamic wave activity began within an hour of the onset of geomagnetic storm conditions. Such behavior is not unexpected. In examining many nights of data we identified a number of occurrences in which the responses were time-synchronous across the fields of view of individual instruments, or even across more than

one instrument. Figures S1 and S2 in Supporting Information S1 provide a very clear example of such an event. Another, albeit less obvious, instance is discernible in Figure 4 at ∼8:30 UT, at both locations, as indicated by large-amplitude responses occurring almost simultaneously across both fields of view. We believe that such events are unlikely to be indicative of propagating waves, because a field of moving wave fronts would result in responses shifted in phase between geographically separated locations; such phase shifts were not observed. As in Figure 3, data from these sites also show a gradual increase in perturbation amplitudes from the zenith toward the horizon indicating the perturbations were associated predominantly with the horizontal wind.

3.1.3. Hemispheric Comparison of Wave Activity

For hemispheric comparison of wave activity, a 2-day period was chosen for which observations were available from Mawson, Antarctica, and Toolik Lake, Alaska. Geomagnetic conditions varied considerably during this period. These two locations were chosen as they lie on broadly similar geographic and geomagnetic latitudes. That is, they are closer in geomagnetic latitude than any other pair of hemispherically opposite sites included in this study. Further, their difference in geomagnetic and geographic latitude is less than the latitudinal width of the auroral zone. Because of their high latitude locations, days on which both sites can observe continuously for multiple hours only occur around the equinox. Further, local time at these two sites differs by 14 hr, which means that lengthy periods of truly coincident observations do not occur because SDIs are only capable of recording sky spectra during darkness. Nevertheless, both sites made observations during the extended period shown in Figure 5. Even though the observations did not overlap in time, we can compare whether the two hemispheres responded similarly to magnetic activity.

On 17 March 2013, exceptionally high amplitude wave oscillations were observed from Toolik Lake, Alaska, and Mawson, Antarctica as a result of highly disturbed geomagnetic activity. Note that these oscillations were plotted using a less sensitive scale than other similar figures in this paper because of the large oscillation amplitudes. These were ∼100 m/s, whereas more typical observed amplitudes were usually ∼50 m/s or less—except, of course, during very active periods. However, on the following day, the geomagnetic disturbance declined at both sites, as did the wave activity. This result suggests that wavelike perturbation amplitudes co-vary in opposite hemispheres. However, testing for actual conjugacy would require observatories in opposite hemispheres that are located on similar longitudes to allow for observations that are truly coincident in time.

3.1.4. Wave Activity Derived From 558 nm Spectra

Figure 6 shows LOS wind oscillations derived from observations from McMurdo Station of both the thermospheric 630 nm red-line emission from the F-region, and the 558 nm green-line emission from the E-region. Strong F-region oscillations were observed throughout the night of 10 April 2018. By contrast, the E-region was mostly placid apart from a sudden packet of oscillations observed beginning at ∼10:00 UT, as seen in the middle panel of Figure 6. Geomagnetic activity was disturbed throughout much of this night. The E-region wave events shown in the middle panel, however, occurred while the magnetometer at Scott Base observed the weakest activity over that whole night. That is, the magnetometer H-component perturbation trace was flatter and was closer to zero than at other times during the observation. Despite this, winds in the E-region manifested the largest amplitude oscillations of any time during the night.

As shown in Figure 7, the 558 nm auroral emission at ∼10–12 UT was associated with elevated and spatially variable Doppler temperatures. This implies that the emission was coming from generally higher altitudes in the E-region, but with considerable height variation across the FoV. Since it is known that strong vertical gradients in horizontal winds occur throughout the E-region (Larsen, 2002), the variability in observation altitude would be expected to be associated with perturbations in measured winds. This effect is likely to have contributed to the burst of oscillations seen after 10 UT. A comparison of the temperature and intensity sky maps (Figures 7 and 8 respectively) shows that the bright regions corresponded to low-energy auroral precipitation (This is because green-line emissions in higher altitudes, corresponding to higher thermospheric temperature, are typically associated with a lower characteristic energy of electron precipitation (Hecht et al., 2006; Kaeppler et al., 2015).). Because of the elevated brightness, it seems likely that this low-energy precipitation would have carried significant energy flux (Gabrielse et al., 2021). This energy would have been deposited higher in the E-region than was the case for most other periods on this night. The heat capacity per unit volume at these higher altitudes is less (due to reduced mass density) than it would have been for the altitudes to which electron precipitation penetrated during other times of this night. The reduced heat capacity may have allowed the soft particle heating to excite

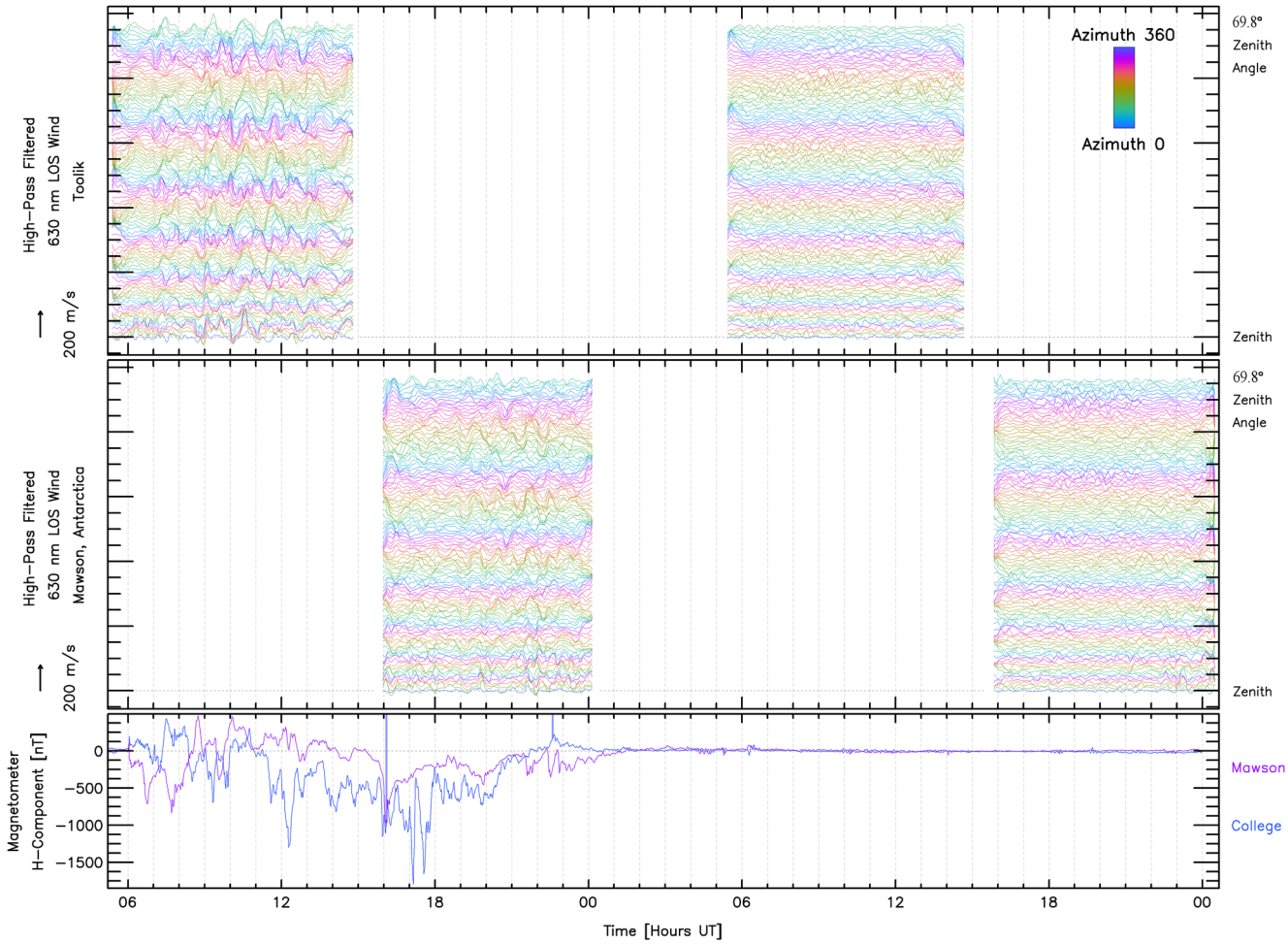

Figure 5. Same as Figure 3 but the upper two panels are showing two days of line-of-sight (LOS) wind data (17–18 March 2013) from Toolik Lake, Alaska, and Mawson, Antarctica. The bottom panel shows the geomagnetic H-component recorded by the magnetometer located at College, Alaska and Mawson, Antarctica, as indicated by the color of the traces. The spikes in the magnetometer trace from College, Alaska near 16 UT and between 22 and 23 UT on 17 March 2013, are most likely due to some interference. On 17 March 2013, the F10.7 index was 124.5 sfu, and three hourly Kp indices were 2+, 7−, 6+, 6−, 6+, 7−, and 6. During the observations on 18 March 2013, the three hourly Kp indices were 3, 2+, 2, 2−, 1+, 1−, 2−, and 1+, and the F10.7 index was 116.6 sfu.

pressure gradients and consequently winds, without requiring electric current, Joule heating, or any associated geomagnetic disturbance. These overall expectations are consistent with the behavior observed. A final contributor to the burst of LOS wind oscillation seen after 10 UT could be the rapidly varying auroral brightness over time, which can sometimes introduce artifacts into Doppler spectra derived from the SDI technique. This mechanism is mostly discussed here for completeness. In this particular case, it is unlikely to be the major source of the observed E-region perturbations. This is because amplitudes of the observed perturbations were the smallest for zones near the zenith, whereas the zenith zones are the ones most sensitive to spectral artifacts of this type. Care should be taken that these three effects (height variations, particle heating, and spectral artifacts) may have accounted for a significant proportion of the observed LOS wind oscillations after 10 UT. The current data do not allow us to determine the relative contributions from these effects versus perturbations caused by atmospheric wave activity. Note that the middle panel of Figure 6 shows another weaker wave enhancement at ∼14 UT. As shown in Figure 7, there was also a corresponding small temperature enhancement during this latter wave event.

Although the magnetometer H-component was never highly disturbed, there was at least modest geomagnetic activity for the whole night (Relevant Kp values are included in the caption for Figure 6.). While large amplitude waves only occurred briefly in the E-region, waves in the F-region occurred with large amplitudes (∼100 m/s) for the whole night. The Scott Base magnetometer data, presented in the bottom panel in Figure 6, showed that the geomagnetic activity was more dynamic earlier in the night before SDI observations began. Presumably, the large

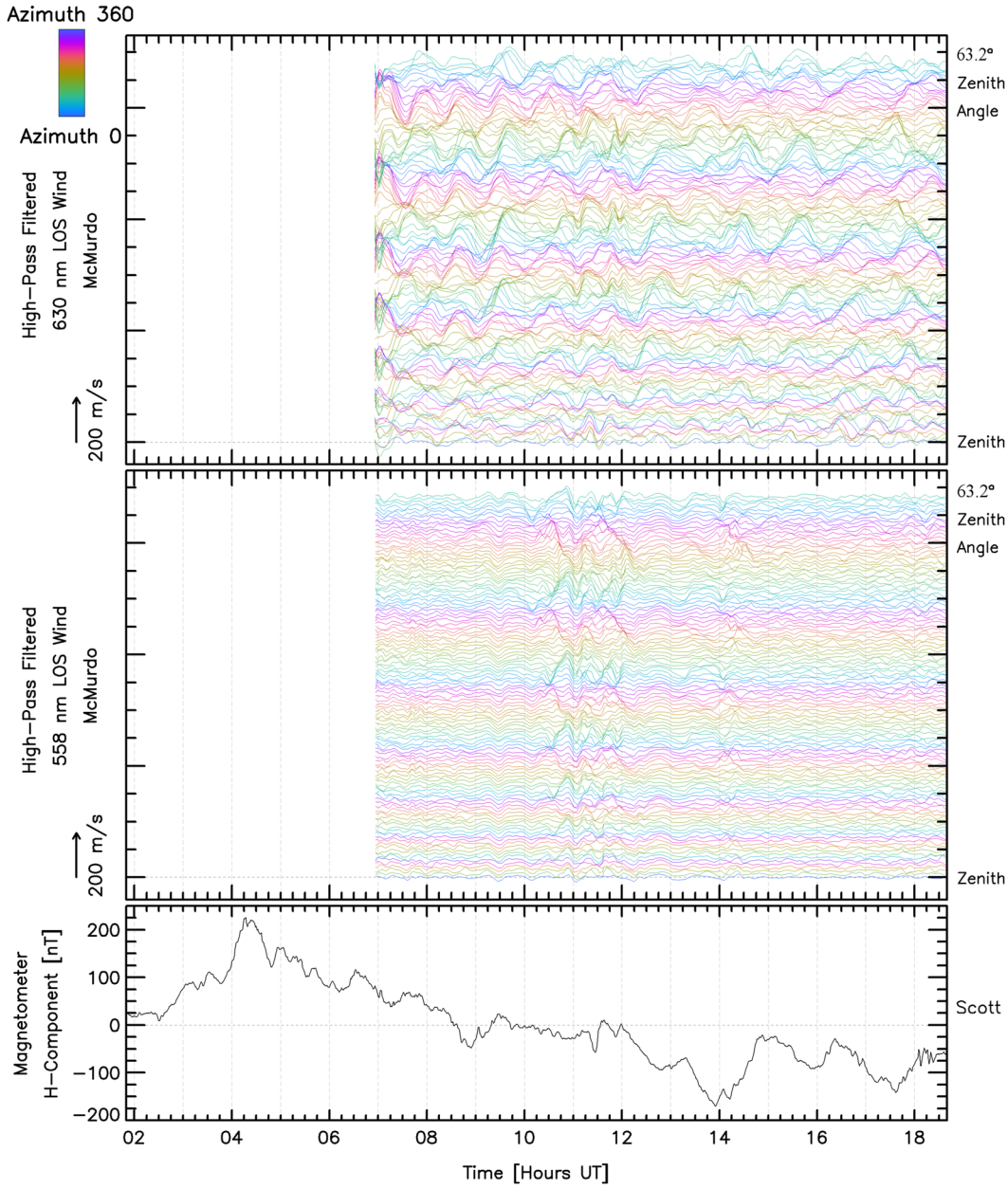

Figure 6. Same as Figure 3 but with top and middle panels respectively showing wave stack plots for F-region and E-region line-of-sight (LOS) wind perturbations observed from McMurdo Station, Antarctica on 10 April 2018. The bottom panel shows the corresponding fluctuations in the magnetic H-component recorded at Scott Base, Antarctica. On this day, the F10.7 index was 68.8 sfu, and three hourly Kp indices during the data period (6–19 UT) were 4, 3−, 3+, 3, and 2+ respectively.

amplitude F-region waves were triggered by this earlier activity. Alternatively, these red-line wind oscillations, with longer wave periods than their E-region counterparts, dissipate slowly and thus could have propagated to the observation location from a different source region (Yiğit & Medvedev, 2019). Oscillation amplitudes increased conspicuously from the zenith toward the horizon for both E-region and F-region perturbations. This zenith angle dependence indicates that the wind perturbations were primarily associated with horizontal winds.

It was initially expected that we would encounter instances of oscillations present at F-region heights as a result of waves propagating up from the lower atmosphere. In this study, the only way to identify potential wave activity driven from below would be to encounter significant wave oscillations during magnetically quiet times. Although wave activity is often present, even at quiet times, it is not possible to determine with any certainty whether small

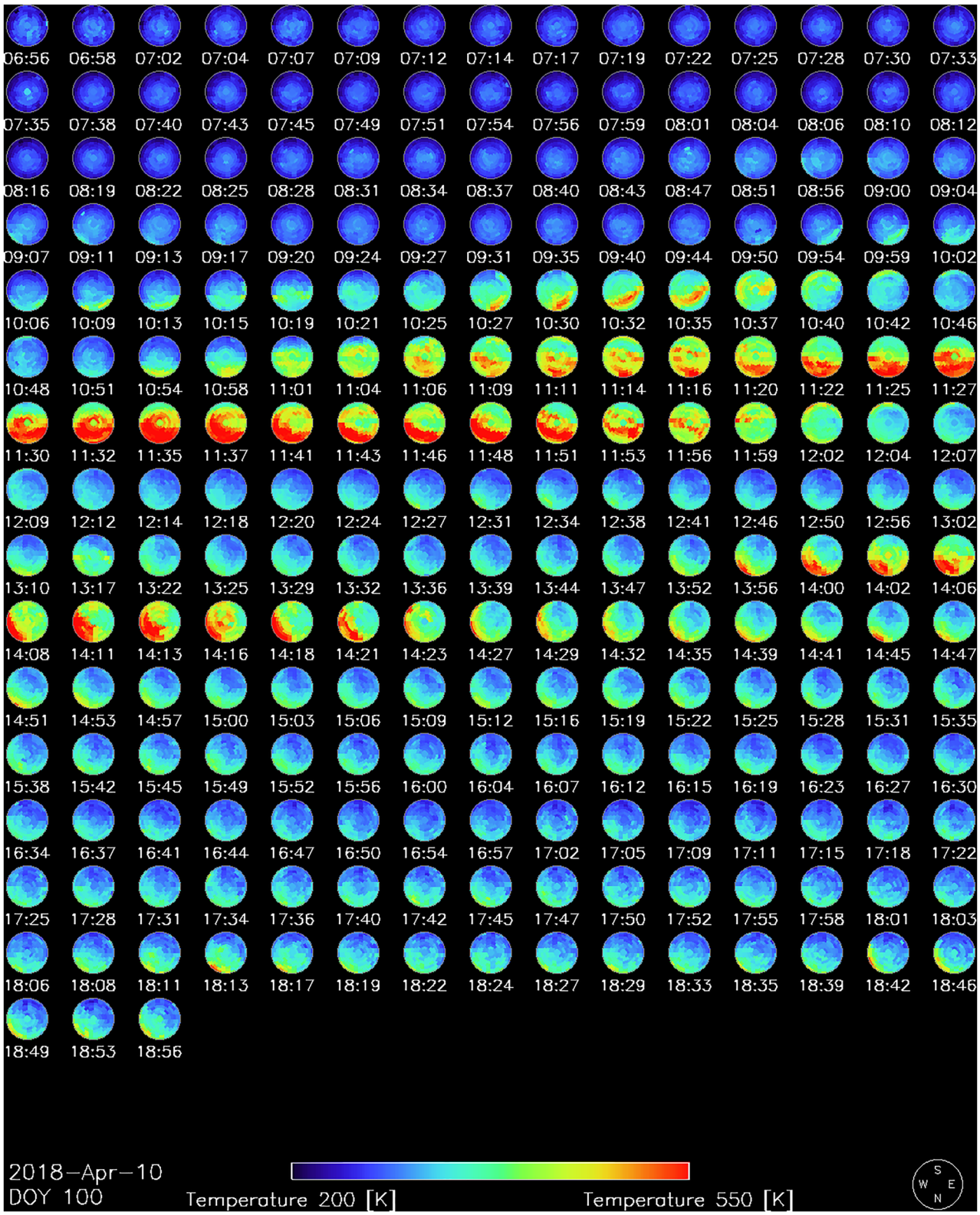

Figure 7. Skymaps of E-region Doppler temperature observed during the night of 10 April 2018, from McMurdo Station, Antarctica. Each circle shows the zenith-centered field of view (all 115 zones) of the Scanning Doppler Imager instrument at the specified time. The edge of each circle corresponds to the horizon (~75° zenith angle). Plot orientation is shown at the bottom right. The horizontal color bar at the bottom of the plot represents the temperature scale. Time in this figure is shown in the units of hours and minutes of the day in UT.

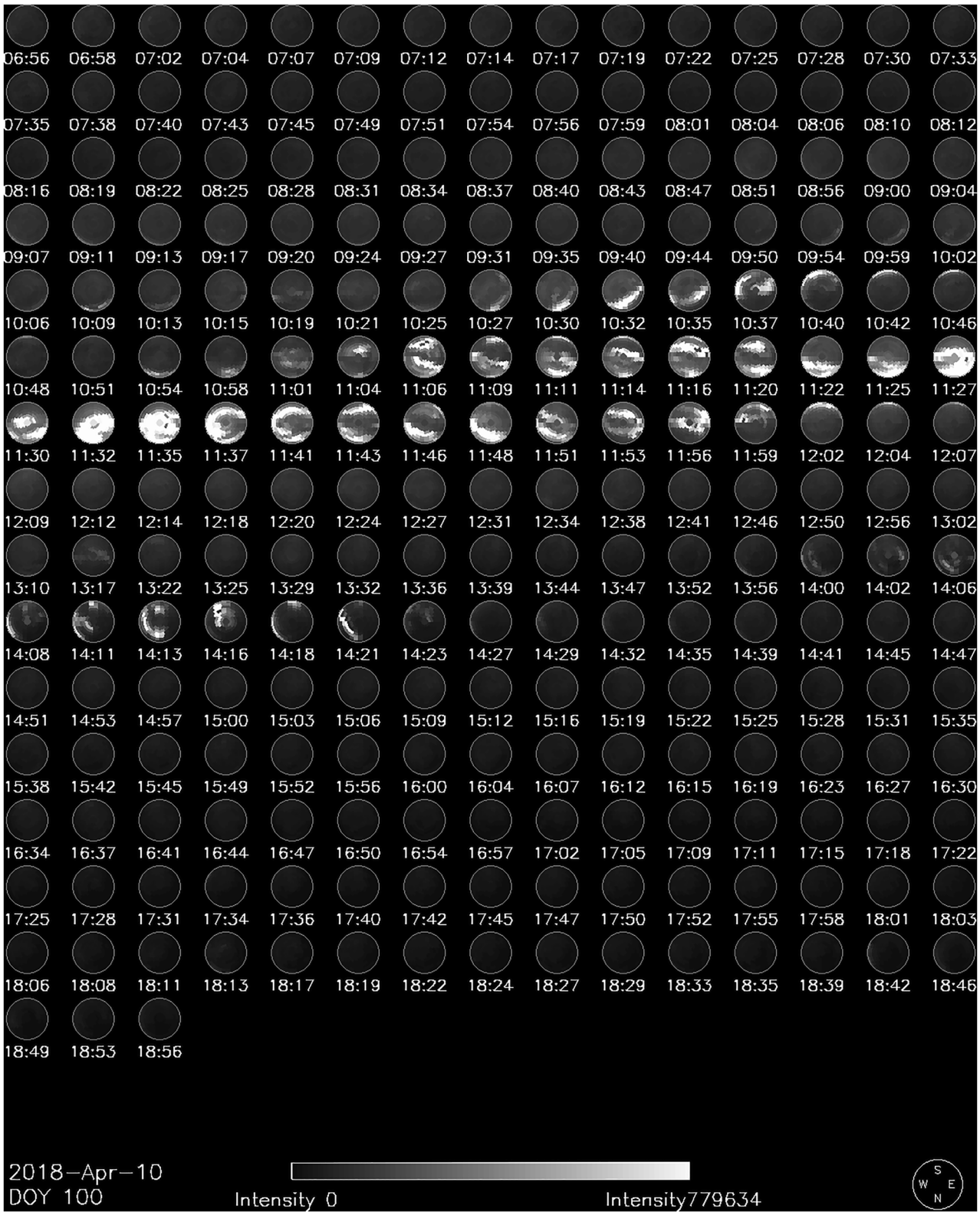

Figure 8. Same as Figure 7 but now showing skymaps (for all 115 zones) of E-region airglow/auroral emission brightness displayed in arbitrary units for the night of 10 April 2018, as observed from McMurdo Station. The horizontal monochrome bar at the bottom of the plot indicates the mapping between relative brightness and gray levels.

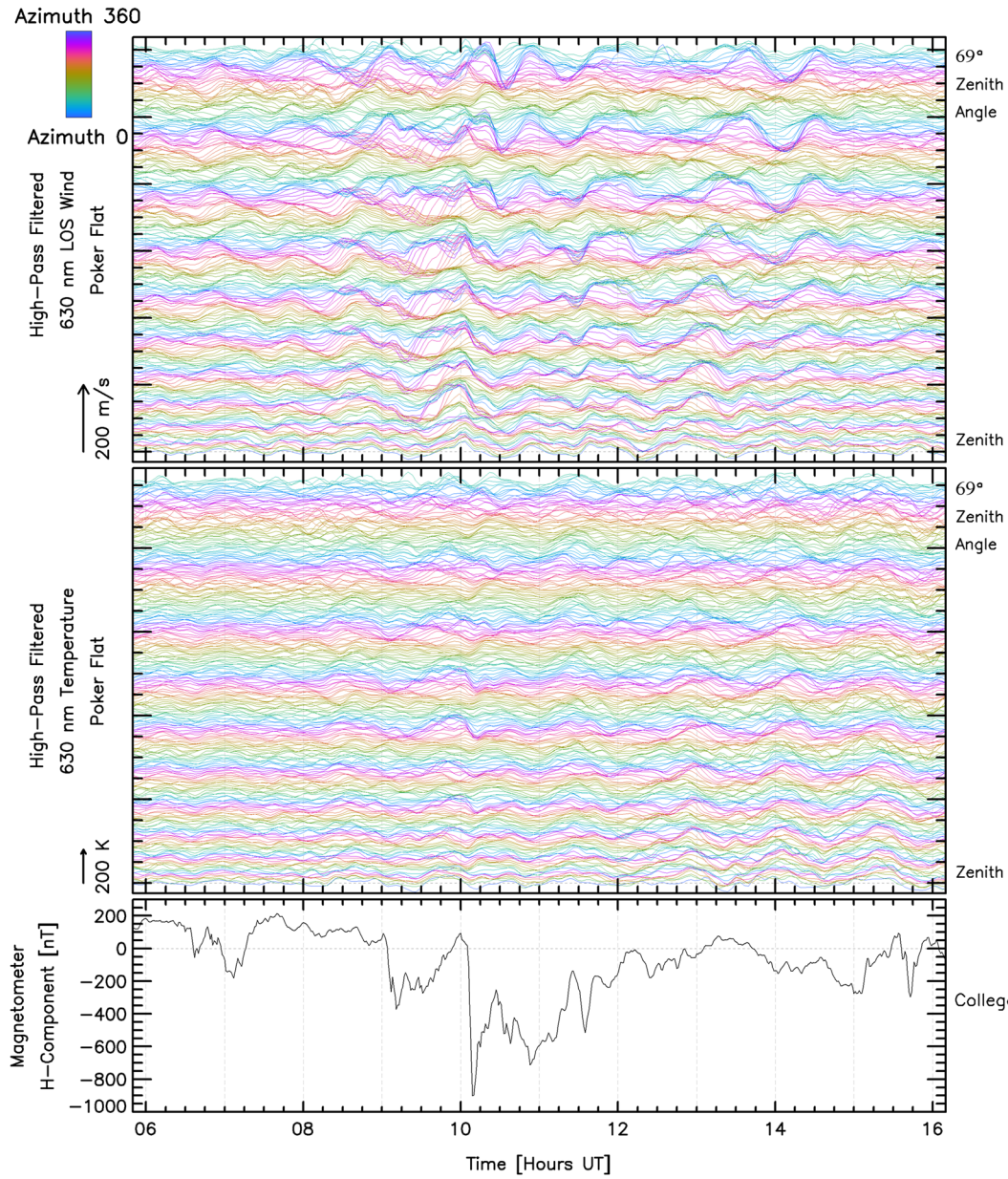

Figure 9. Same as Figure 4, but in this case showing wind and temperature oscillations as observed from Poker Flat, Alaska during the night of 7 November 2017, along with the corresponding magnetometer H-component recorded at College, Alaska. The F10.7 on this day was 67.0 sfu, and the three hourly Kp indices during (6–16) UT were 3+, 5−, 4−, and 4−.

amplitude waves arose as a result of forcing from below, as opposed to being due to in-situ forcing. Of course observation of a large-amplitude wave packet during very quiet geomagnetic conditions would more strongly suggest that these waves were excited from below. However, no clear instances of large amplitude waves during geomagnetically quiet times were found in the data examined for this study. Overall, it is not possible from these data to unambiguously identify instances of forcing from below. Nevertheless, clear examples may occur after more extensive observations. Further, we may well have observed waves excited from below but have been unable to establish their origin definitively.

3.1.5. Concurrent Wavelike Oscillations in Temperatures and LOS Winds

In addition to extracting thermospheric wind oscillations from the SDI spectra, wavelike perturbations in temperature have also been obtained. Figure 9 shows simultaneous perturbations in temperatures and LOS winds during

the night of 7 November 2017, observed from Poker Flat, Alaska. Signatures of time-synchronous events, appearing as simultaneous responses occurring across almost the whole all-sky FoV, are evident on several occasions. For example, the large amplitude perturbations seen in both temperature and wind at ~10 UT are not signatures of propagating waves. By contrast, propagating waves would be characterized by phase progressions among the oscillations recorded along different look directions. Numerous instances of such phase progressions are noticeable in the LOS wind oscillations shown in Figure 9. An increase in the amplitude of wind oscillations toward the horizon, as seen in Figure 9 is consistent with the expectation that the perturbations were associated mostly with the horizontal wind. Note that, on this particular day, the all-sky FoV of the SDI at Poker Flat was divided into a total of 261 zones, resulting in 261 traces for wind, and similarly for temperature (By contrast, the regular observing mode only divides the all-sky FoV into 115 zones.). There was a high correlation between the overall wave activity throughout this night with the geomagnetic activity shown in the bottom panel. Similar wave activity was observed at Toolik, Alaska as well on this night (not shown here).

Throughout the entire data set examined, magnitudes of observed oscillation amplitudes relative to experimental uncertainties were typically smaller for temperatures than they were for winds. One consequence of this is that there were fewer instances within the entire data set of unambiguous detection of wavelike activity in temperature, regardless of period. This difference is most extreme for shorter-period waves, for which oscillations were not typically detected in temperature, again presumably because the amplitude of any short-period perturbations would not be large enough to be discernible against background noise. At times when temperature oscillations were detected, their amplitudes did not increase significantly from the zenith to the horizon. This is unlike the behavior observed for wind oscillations. This lack of dependence on the zenith angle for the temperature oscillation amplitudes is as expected for a scalar quantity.

By having both temperature and LOS wind perturbations, in principle, the GW polarization relations could be used to infer additional characteristics of the underlying waves. However, the implementation of this analysis is not straightforward, because only the LOS component of the wind oscillations has been measured.

3.2. Sliding Window Spectral Decomposition

As noted above, several previous studies have presented typical ranges of parameters for thermospheric GWs. In this section, estimates of temporal periods are derived from the current data to determine whether the oscillations observed here are consistent with previous observations. In the subsequent discussion, we will also consider the consistency of the horizontal wavelength, horizontal phase speeds, and relative amplitudes of the wind and temperature perturbations.

During any given night, it is to be expected that the observed wave period would vary from zone to zone and over time. Therefore, a procedure was needed that could be applied independently to a given zone and could resolve how the wave periods varied during the night. To resolve time variations, subsets of the time series for a given zone were taken using a sliding window of 180 min duration. The sliding window was initially centered at the time of the first measurement that occurred more than one-half of the window time after the start of observations and included all points within one-half of the window time from the center. A power spectrum of the data within the window was then calculated using the Lomb-Scargle technique (Lomb, 1976; Scargle, 1982). After each power spectrum calculation, the time series point chosen to define the window's center time was advanced by one. The final result was a set of power spectral density profiles calculated as a function of the central times of the sampling windows.

However, the resulting power spectral measurements were distributed non-uniformly in time. SDI instruments self-adjust their exposure time depending on the brightness of the optical airglow/auroral emission. Since the brightness changes over time, the corresponding temperature and LOS wind observations are not uniformly spaced in time, which is why the Lomb-Scargle approach was used rather than the more common fast Fourier transform method.

Example results are shown for a selected day in Figures 10–13. To render these data as a false-color 2-D image, the power spectra were thus interpolated onto a regular time grid. Overall, this allowed us to plot, for any selected zone, the power spectral density as a function of wave period and universal time during the night. This result is referred to as a "dynamic spectrum."

Note that the all-sky FoV is typically divided into 115 different zones. For a given night, a separate dynamic spectrum can be produced for each of those zones, or, alternatively, an all-sky dynamic spectrum can be generated by averaging the power spectra from each zone. In the discussion below, one example is presented of the dynamic spectrum computed from a single zone over one night, for both red-line and green-line observations. The corresponding

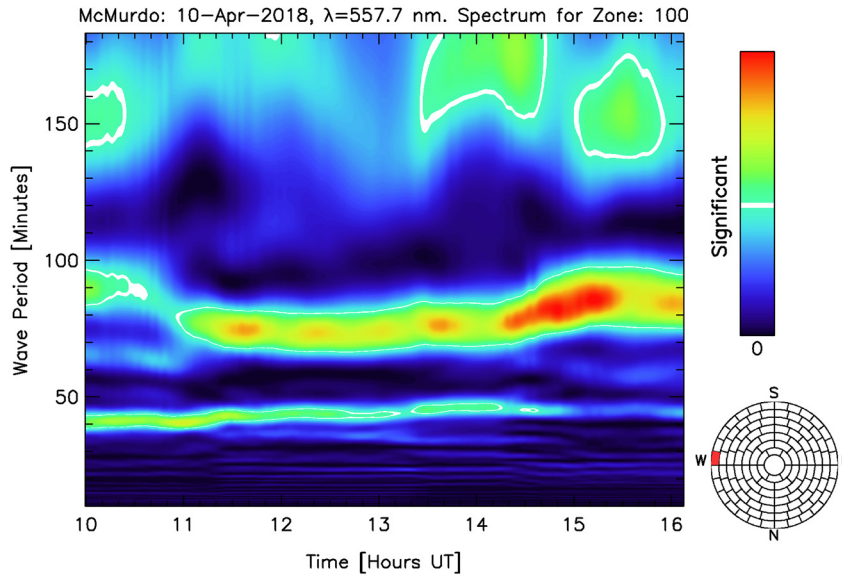

Figure 10. Dynamic Spectrum corresponding to zone number 100 for E-region winds during the night of 10 April 2018, as observed from McMurdo Station, Antarctica. Power spectral density (in arbitrary units) is represented using blue through red hues, as indicated by the color scale bar at the right. The white horizontal line on the color bar indicates the level above which there is less than 5% probability that power calculated by the Lomb-Scargle analysis was derived solely from random noise. Power at this level, plotted in white, forms contours that segregate regions of significant power from the noise. The small zone map at the bottom right indicates (in red highlighting) the zone chosen for the spectral decomposition.

all-sky averaged dynamic spectra for both (red-line and green-line) observations on the same night are also presented. It is important to realize that the all-sky plots were produced by averaging the power spectra, rather than computing a single power spectrum from the LOS wind time series averaged over all zones. Because the wind component used here is aligned with the instrumental LOS, averaging this component over the whole sky would be undesirable, as this would typically suppress most of the geophysical information present in the original measurements.

3.2.1. Spectral Decomposition of E-Region LOS Wind Oscillations

Figures 10 and 11 show examples of dynamic spectra for the night of 10 April 2018, corresponding to E-region winds as observed from McMurdo Station, Antarctica. In these figures, *x*-axes represent universal time in hours

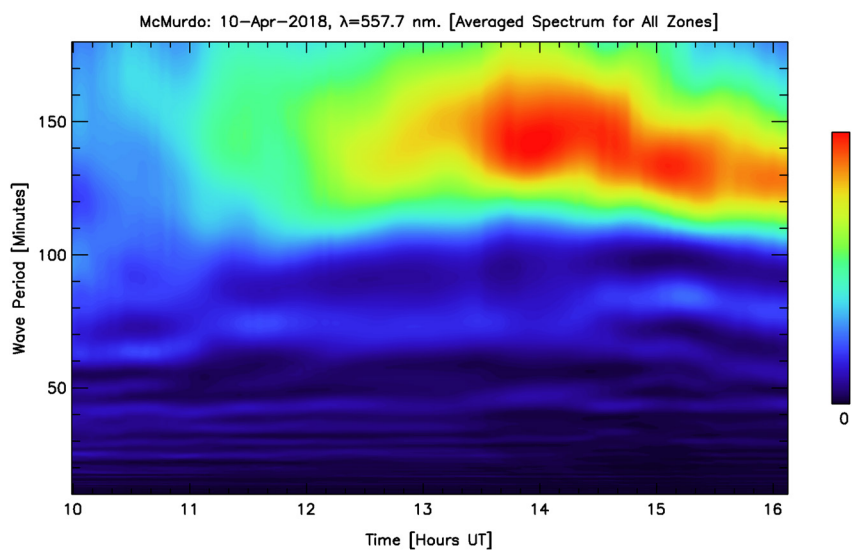

Figure 11. Green-line periodogram for the same day as Figure 10, but averaged over the whole field of view. In this case, the power spectral densities were calculated for each zone during the night and then averaged.

while the *y*-axes represent wave periods in minutes. The fill colors are related to the power spectral density in arbitrary units, as indicated by the color bar on the right. The white horizontal indicator line in the color bar represents the level above which the estimated power spectral density is greater than the noise, to a statistical confidence of 95%.

Figure 10 represents a single zone (zone number 100), centered approximately at geographic longitude: 165.53° and geographic latitude: −75.72°. This particular zone was chosen because the range of periods containing significant power varied considerably during the observations in this zone. Several spectral features appeared in this zone during the observations on this day. By contrast, there were other zones where the band of significant power remained relatively constant over time. The location of the selected zone within the all-sky FoV is shown at the bottom right by red highlighting in a small zone map. In this zone, wave periods during the observation ranged from ∼30 min to as long as more than ∼180 min. Oscillations with periods centered around 85 min prevailed for more than 5 hr (which is more than 3 wave periods) during the night.

Figure 11 shows the dynamic spectrum averaged over all the 115 zones for E-region winds observed on the same night and from the same location as in Figure 10. This all-sky dynamic spectrum is rather simply structured, with maximum power centered around an oscillation period of ∼150 min. Shorter-period oscillations, such as those observed in zone 100 (Figure 10), did not appear in the all-sky dynamic spectrum. These short-period oscillations were examined across all the zones during the night and it was found that those oscillations were present only in about 20 zones that were away from the zenith in the western portion of the FoV. Further, shorter-period oscillations were observed to have smaller amplitudes than longer-period oscillations. Subsequently, such weaker oscillations tended to average to zero across all zones. The fact that a cluster of waves with a band of periods prevailed only in a small number of zones (i.e., ∼20) strongly suggests that the corresponding oscillations were not instrumental artifacts. The optical configuration of the SDI instruments is such that signal originating from every viewing zone illuminates the entire aperture of the etalon. This means that any artifacts resulting from unstable etalon behavior would affect all zones. There is no mechanism by which etalon instability could only impact a small subset of zones. This means that oscillations seen in a small subset of zones are unlikely to be of instrumental origin.

On this night, the majority of the power was centered among oscillations with periods in the range spanning ∼120–160 min. The long-period cutoff appeared less sharp relative to that for the shorter-period oscillations. However, this is most likely a consequence of the longest periods shown in Figure 10 becoming comparable to the width of the sliding time window, which has the effect of reducing the spectral resolution achievable for the longest periods shown. It is clear that longer-period oscillations, centered around 150 min, such as those detected in zone 100, were present in the majority of the zones because the same signatures were visible in the all-sky dynamic spectrum shown in Figure 11 as well.

3.2.2. Spectral Decomposition of F-Region LOS Wind Oscillations

Figures 12 and 13 show dynamic spectra for F-region winds as observed from McMurdo Station, Antarctica during the same night (i.e., 10 April 2018) as the green-line winds presented earlier. Figure 12 represents the dynamic spectrum derived from just one zone, zone number 52, centered approximately at geographic longitude: 165.04° and geographic latitude: −75.57°. This zone at F-region altitude corresponds to a similar geographic location as zone 100 for E-region observation shown earlier. For this zone, wave periods carrying significant power ranged over the whole night from ∼60 min to more than 180 min. However, most of the time, the wave periods of the statistically meaningful oscillations were more confined, spanning only the approximate range from 90 to 180 min. Although wave power was detected at times from each altitude at periods shorter than those mentioned above, such occasional occurrences are likely due to the high-end tail of the noise distribution, given that the indicated confidence level is rarely substantially greater than the chosen threshold of 95%. The most significant power was observed shortly after 12 UT for periods centered around 90 min and after ∼13 UT for periods centered around 170 min. As was the case of the E-region wind oscillations shown previously, the Lomb-Scargle analysis yielded lower spectral resolution for longer periods (again as expected). Oscillations with periods less than ∼60 min at F-region altitudes were rarely detected in the SDI data. This is understood to be the consequence of the mechanisms for the generation and dissipation of waves in the F-region. These estimates lie within the range previously reported (e.g., Miyoshi et al., 2018). However, spectral analysis of the time series of LOS winds derived from 558 nm emission (which originates at lower E-region heights) did commonly identify shorter-period (as short as ∼30 min) oscillations (e.g., Figure 10).

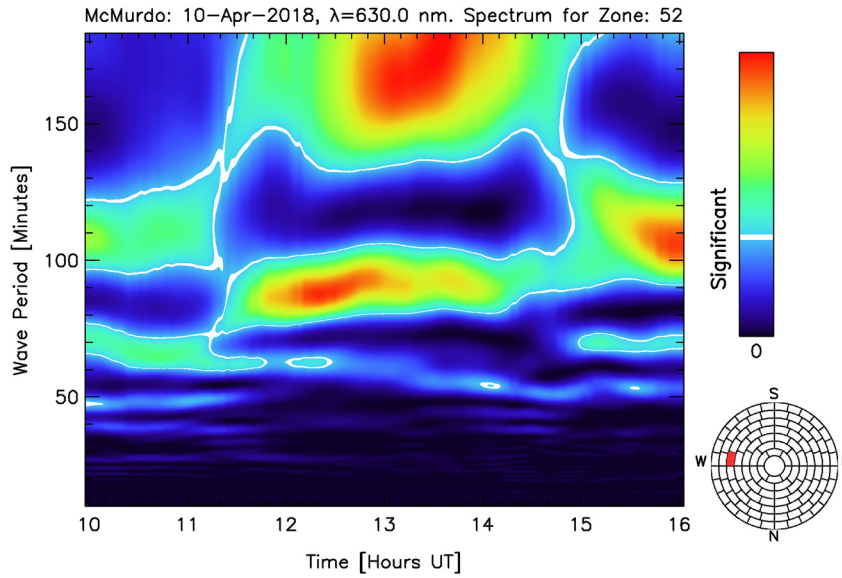

Figure 12. Same as Figure 10 but corresponding to F-region winds as observed from McMurdo Station, Antarctica on 10 April 2018, in zone number 52. The zone map at the bottom right shows, in red highlighting, the zone chosen for this dynamic spectrum plot. As in Figure 10, white contours separate the region of significant power from the noise.

Figure 13 shows the dynamic spectrum for F-region winds averaged over the whole FoV of the SDI instrument located at the McMurdo Station during the night of 10 April 2018. As in the previous case of E-region winds, some of the weak oscillations seen in a single zone averaged to zero in the all-sky dynamic spectra. The band of red and green colors apparent in this plot reflects the large-scale picture of the wave activity during the night. The lowest significant period detected in the all-sky F-region LOS wind periodogram on this day was ~60 min. As before, the long-period boundary of the band of statistically significant power for F-region wind oscillations was not as sharp as the short-period boundary, again presumably as a consequence of limited spectral resolution for long periods. Periods where the power spectral density was prominent in zone 52 (Figure 12) were largely conspicuous in the all-sky dynamic spectrum as well, indicating that these oscillations were present in most zones.

All-sky averaged periodograms shown in Figures 11 and 13 depend on both the temporal and spatial distribution of the perturbations. Shorter period fluctuations are likely to be more effectively suppressed by the all-sky

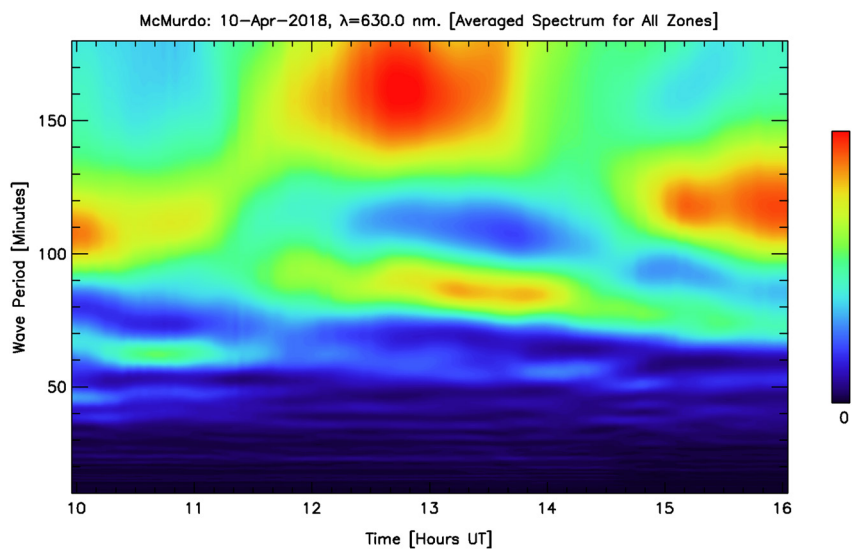

Figure 13. Same as Figure 11 but for F-region wind oscillations.

averaging if they are typically more spatially localized. We presume that this is indeed why the E-region all-sky periodogram contains less power at shorter periods than the corresponding all-sky result in the F-region, even though individual zones may contain more power at shorter periods.

Note that the dynamic spectra showed substantial variability in wave periods from zone to zone. Wave periods that were statistically significant in a specific viewing zone were not necessarily significant in the all-sky dynamic spectrum.

In principle, these instruments could introduce oscillatory artifacts, for example, due to oscillations in etalon control parameters such as temperature. However, as discussed previously, any such instrumental oscillations would almost certainly affect all zones similarly. The fact that unique oscillations were seen only in a subset of the zones strongly suggests that these spectra were not instrumental artifacts. On some nights, the Lomb-Scargle analysis of data from some zones showed no periods with statistically significant wave power. Such instances were rare but did occur for some days that are included in this study.

4. Discussion

4.1. Artifacts Due To E-Region Emission Height Variation

Significant oscillations compared to the noise were observed on most nights of good data. By contrast, the SDI data contained fewer instances of clear wavelike oscillations in either F-region temperature or E-region LOS winds. Even though the 558 nm Doppler shift and Doppler width are accurately determined by the instrument with a high signal-to-noise ratio, interpretation of these quantities is complicated by the changing height of the green-line emission layer. In the case of deriving temperatures from Doppler widths, the vertical temperature gradient is so strong in the E-region that the dominant perturbations in high pass filtered 558 nm temperature time series arise simply because of the emission height variations due to changing characteristic energy of the auroral precipitation that excites the emission. Thus, although oscillations were seen in E-region temperatures, we presume that these mostly would have been due to changes in the aurora rather than the actual fluctuations in the background temperature at a constant height. In the case of 558 nm LOS wind measurements, the vertical gradients of horizontal wind in the E-region can also be strong (Branning et al., 2022; Larsen, 2002), which means that height variations of the emission layer may add artifacts to the high pass filtered LOS wind time series that could, at times, dominate over other signals, such as those that might indicate the presence of atmospheric waves. Periods when such artifacts appear can be easily identified as “bursts” of noise in the wind time series correlated with periods when the 558 nm Doppler temperature is changing rapidly. An example of such behavior is shown in Figure 14. In this figure, the fitted zonal wind is noisy and variable when the fitted temperature is more variable. Note that much of the variability indicated by the wind error bars arises not because the fitted winds have large uncertainty but because the fitted wind field is non-uniform. Temperature variations indicate changes in the emission height—and that could mean the measured winds would change if there was a strong vertical gradient in the wind field. In this experiment, there is no way to determine whether strong vertical gradients were present—but the figure at least shows that some of the wind variability could be associated with height changes. Such changes, if they do occur, would contribute to perturbations in the wave plots. However, an examination of roughly 20 years of 558 nm SDI data shows that the strength of this contribution can be quite variable. Overall, it is thus not surprising that E-region wind oscillations look noisier in the SDI data than those generally observed for F-region winds.

4.2. Qualitative Testing of the Plausibility of Wave Interpretation

SDI instruments have multiple viewing zones that project to an extended geographic region in the thermosphere. For waves propagating across the instrument's FoV, systematic delays are expected between the times at which a given phase front would cross viewing zones that are separated with respect to each other along the direction of wave propagation. There should thus be systematic phase differences between perturbations observed by the individual zones, with the particular pattern of phase differences being characteristic of the speed and direction of the wave's phase propagation. Further, the observed LOS wind oscillation is typically modulated in part by the viewing azimuth. This is because the contribution to the observed wave perturbation is modulated by the dot product of the viewing azimuth direction and the direction of horizontal motion associated with the wave. Note that no such viewing azimuth dependence applies to the LOS component of vertical wave oscillations. Rather, this contribution is instead modulated by the cosine of the observing zenith angle.

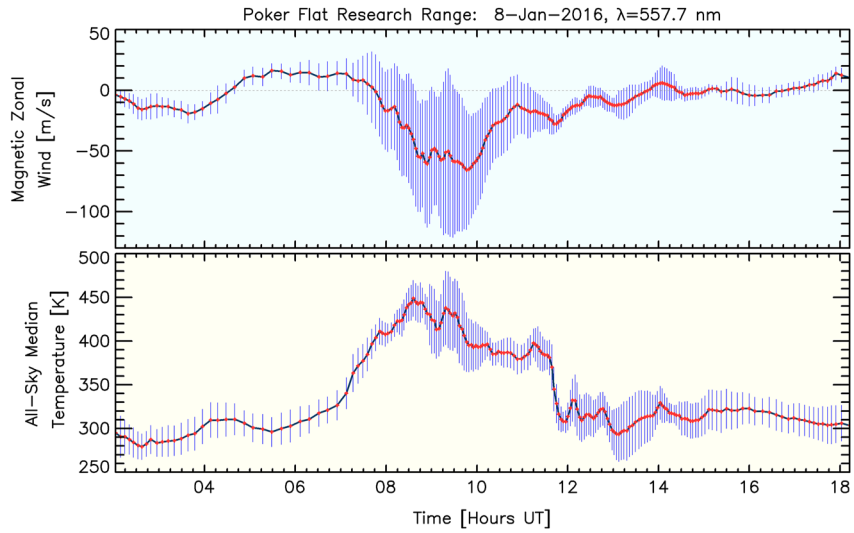

Figure 14. Fitted temperatures and winds derived from 558 nm spectra for 8 January 2016, at Poker Flat. The top and bottom panels respectively show the fitted zonal wind speeds and all-sky median temperatures as a function of time. In both panels, the "error bars" show the standard deviation of the corresponding 115 values of the fitted quantity at each observing time. Thus, the error bars are not solely indicating statistical uncertainty in the measurements—in many cases, longer error bars arise because of true geophysical variability across the field of view (however, statistical uncertainty will always have some contribution).

If wind perturbations occurring in the atmosphere were only in the horizontal components, the amplitude of the LOS component of this oscillation would be zero when looking in the zenith and, for other look directions, it would increase in proportion to the sine of the zenith angle. In most instances, this general behavior was observed for the LOS wind, although the amplitude of the oscillation in the zenith zone was almost never seen to drop entirely to zero. Usually, small but non-zero oscillation amplitudes were observed in the zenith zone, with the amplitude of these oscillations increasing with zenith angles (as expected) out to a maximum near the horizon. These characteristics indicate that the wind perturbations had both horizontal and vertical components associated with them, with the horizontal component typically being larger. The observed systematic dependence of LOS wind perturbation amplitude on the zenith angle would be extremely unlikely to arise purely because of instrumental artifacts. Instead, observed perturbations are almost certainly of geophysical origin. Temperature oscillations are, by contrast, scalar quantities that would not manifest any amplitude dependence on zenith or azimuth angle—which was largely consistent with the actual behavior observed.

Moreover, for a uniform field of monochromatic plane phase fronts, and a given zenith angle, there would be a pair of diametrically opposite azimuths for which the LOS components of the horizontal wind oscillation amplitudes would maximize, and they would be zero when viewing perpendicular to those azimuths. However, as depicted in Figure 15 (and in most other cases inspected), such simple and systematic azimuthal variation of perturbation amplitudes were not observed. It is inferred from this that the actual wind perturbations in the SDI data were usually not due to a uniform field of monochromatic waves in the horizontal wind. Rather, the actual wave fields in the thermosphere must always be more complicated indicating, for any given time, the presence of a range of periods and multiple propagation directions within the FoV. Nevertheless, Figure 15 clearly shows that the wind oscillation phase does vary with azimuth, as expected for a geophysical field of propagating waves.

As expected, instances of relative phase differences between oscillations in different zones were frequently seen. However, there were other times when no phase differences between oscillations were seen regardless of the look azimuths and look elevations. These events were characterized by large amplitude fluctuations occurring almost time-synchronously across much of the FoV. Such attributes arise in the SDI data as shown, for example, in the top two panels of Figure 4 at ∼8:30 UT and in the 558 nm wind panel of Figure 6 at ∼11 UT. These time-synchronous responses cannot be signatures of propagating waves. Rather, two possible ways in which such signatures could arise in the SDI data can be postulated.

First, impulsive changes in magnetospheric forcing can impact a wide geographic area of the thermosphere simultaneously. These signatures could thus indicate directly-driven atmospheric perturbations responding

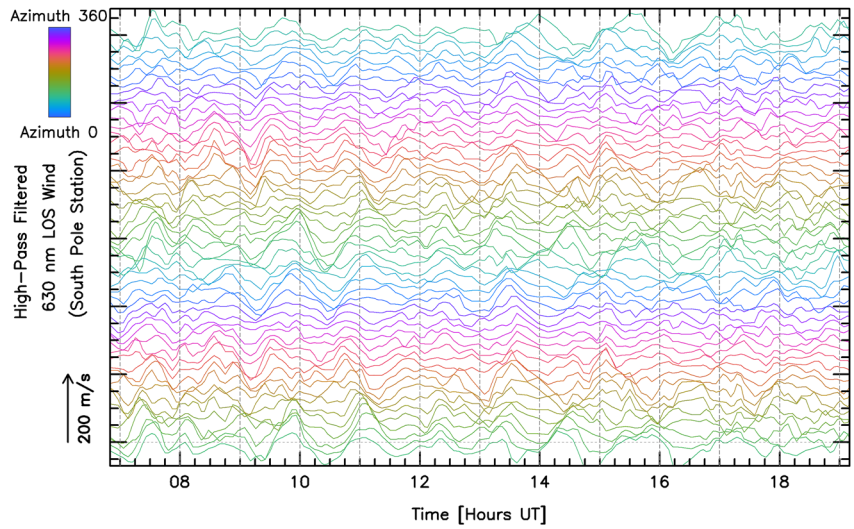

Figure 15. High-pass filtered line-of-sight (LOS) wind perturbations for selected zones spanning the two outermost rings of the Scanning Doppler Imager field of view (zones 63–114) on 10 April 2018, as observed from the South Pole Station (same day as in the middle panel of Figure 3). By selecting just the two outermost rings, there are fewer traces in the figure. This allows individual traces to be discerned along with the relationships between successive traces.

simultaneously over a wide geographic area to sudden changes in magnetospheric forcing. The result would be a time-synchronous response across most if not all of the SDI instrument's FoV. It is noted, however, that even if the wind changes time-synchronously, amplitude and phase shifts in the observed LOS wind components are still expected due to the projection angle with varying viewing azimuth. (No such azimuth dependency is expected for temperature perturbations.)

A second (and perhaps more significant) issue arises because sudden changes in auroral precipitation can cause this remote sensing technique to introduce artifacts in the measured winds and temperatures. For example, the time variation of emission brightness can distort recorded spectra because of the way the etalon scans over time, particularly for zones near the zenith. More importantly, as described previously, the altitude of the observed emission can change in response to changing characteristic energy of auroral precipitation. If the observed quantity (wind or temperature) varies with height in the background atmosphere, then the change in characteristic energy will cause changes in the measurements that do not reflect any actual temporal change in the real atmosphere (McCormac et al., 1987; Sica et al., 1986).

Time-synchronous events typically occurred superposed upon a preexisting ambient wave field. Nevertheless, the time-synchronous events almost always were observed during times of substantial impulsive auroral and geomagnetic forcing of the atmosphere. This forcing often excited significant oscillations that were resolvable for several hours after the initial event. Thus, even though the time-synchronous perturbations do not appear to themselves be signatures of wave perturbations, they usually indicated the onset of forcing events that did produce subsequently observable waves.

Time-synchronous perturbations can be identified readily in the SDI data but may not be as conspicuous to an instrument with observations in a single look direction. Observations based on a single look direction would be unable to distinguish between traveling waves and time-synchronous non-wavelike oscillations, due to the inability to track phase shifts among the different look directions. This could lead to every oscillation being interpreted as a signature of a traveling wave. However, as explained above, this current study has shown that there are many instances when such an assumption would be likely to be incorrect, at least for large perturbations observed in auroral latitudes. We, therefore, caution that inferences regarding wave activity that are based on Doppler spectral observations incorporating only one look direction might be biased by artifacts associated with the types of time-synchronous responses that have been identified here.

As discussed in earlier sections, waves in the thermosphere do not exclusively originate in situ. Some portion of the wave spectrum is caused by driving that occurs in the lower atmosphere, with perturbations subsequently

propagating up to the thermosphere, albeit possibly after one or more instances of breaking and exciting secondary waves (Smith et al., 2013; Vadas et al., 2018). During this process of wave breaking and critical layer filtering, the original shorter-period waves typically fail to reach thermospheric heights. Further, the dissipation of waves as a result of rapid diffusion suppresses short-period waves in the F-region (Fritts & Alexander, 2003). Based on these considerations, the resulting F-region wind oscillations would be expected to be smoother (with less power at high frequencies) than the corresponding E-region oscillations. The observations were indeed consistent with this expectation.

4.3. Quantitative Consistency Tests

As noted, it is difficult to know the extent to which the oscillations observed here are due to atmospheric GWs, versus other geophysical processes or (possibly) instrumental artifacts. However, one potential "back-of-the-envelope" diagnostic is to test whether relations between observed perturbations in the horizontal wind, vertical wind, and temperature are at least not inconsistent with theoretical expectations for thermospheric GWs. Application of simplified GW polarization relations for a harmonic oscillation (e.g., Hines, 1960) predicts the following relationships between the various wave perturbation amplitudes and wave parameters

$$\frac{u'}{\omega k_x k_z C^2} = \frac{w'}{-\omega k_x^2 C^2} = \frac{\rho'/\overline{\rho}}{i(\gamma-1)g k_x^2}, \tag{1}$$

where u' and w' are the amplitudes of the wave's horizontal and vertical oscillations respectively, $\rho'/\overline{\rho}$ is the fractional mass density perturbation amplitude, ω is the intrinsic (angular) frequency of the wave oscillation, k_x and k_z are the horizontal and vertical wave numbers, g is the acceleration due to Earth's gravity, γ is the adiabatic constant (with a value of 5/3 for a monatomic gas), and $C = \sqrt{\gamma g H}$ is the speed of phase propagation for sound waves with H being the scale height. Also, i is $\sqrt{-1}$, which merely indicates that the density oscillations are 90° out of phase with the wind oscillations.

Assuming the relative temperature perturbation amplitude $T'/\overline{T}$ is the same as the relative density amplitude, and writing the Brunt-Väisälä frequency as

$$\omega_b \simeq \sqrt{\frac{\gamma-1}{\gamma}\frac{g}{H}}, \tag{2}$$

Here, we have assumed that the relative pressure perturbations were negligible, which is reasonable for the periods we observed.

Equation 1 can be rearranged to give

$$\frac{T'}{\overline{T}} \simeq \frac{\omega_b^2}{g\omega} w', \tag{3}$$

$$\text{and } \frac{k_x}{k_z} = \frac{w'}{u'}, \tag{4}$$

The quantities u', w', T', $\overline{T}$, and ω obviously vary considerably among the data examples presented here. For each of these parameters, the largest observed perturbation amplitudes in this study were a factor of ~5 times stronger than the smallest observed perturbation amplitude. Notwithstanding this variability, the polarization relations should hold for any particular wave packet. Therefore, we have examined the relationships between wave parameters for representative data, in this case, taken from McMurdo station on the night of 10 April 2018. We have applied a relatively narrow band-pass filter to more clearly show the wave perturbations (Figure 16). Perturbation amplitudes were derived from the mean absolute value of this narrow band-pass filtered time series over the whole night after accounting for a mathematical factor that is needed to convert these means to wave amplitudes. Results were $u' \simeq 34$ ms^{-1} and $w' \simeq 9$ ms^{-1}. Here, w' was estimated from the mean absolute value of the LOS wind oscillation in the zenith zone. The amplitude of horizontal wind oscillation was calculated from the mean absolute values of the LOS wind oscillation for those outer zones in which the oscillation amplitudes as a function of azimuth maximized. In these zones, horizontal motion was azimuthally aligned with the instrumental look direction. Note that the calculation of horizontal wind amplitudes also accounted for the dependency of LOS

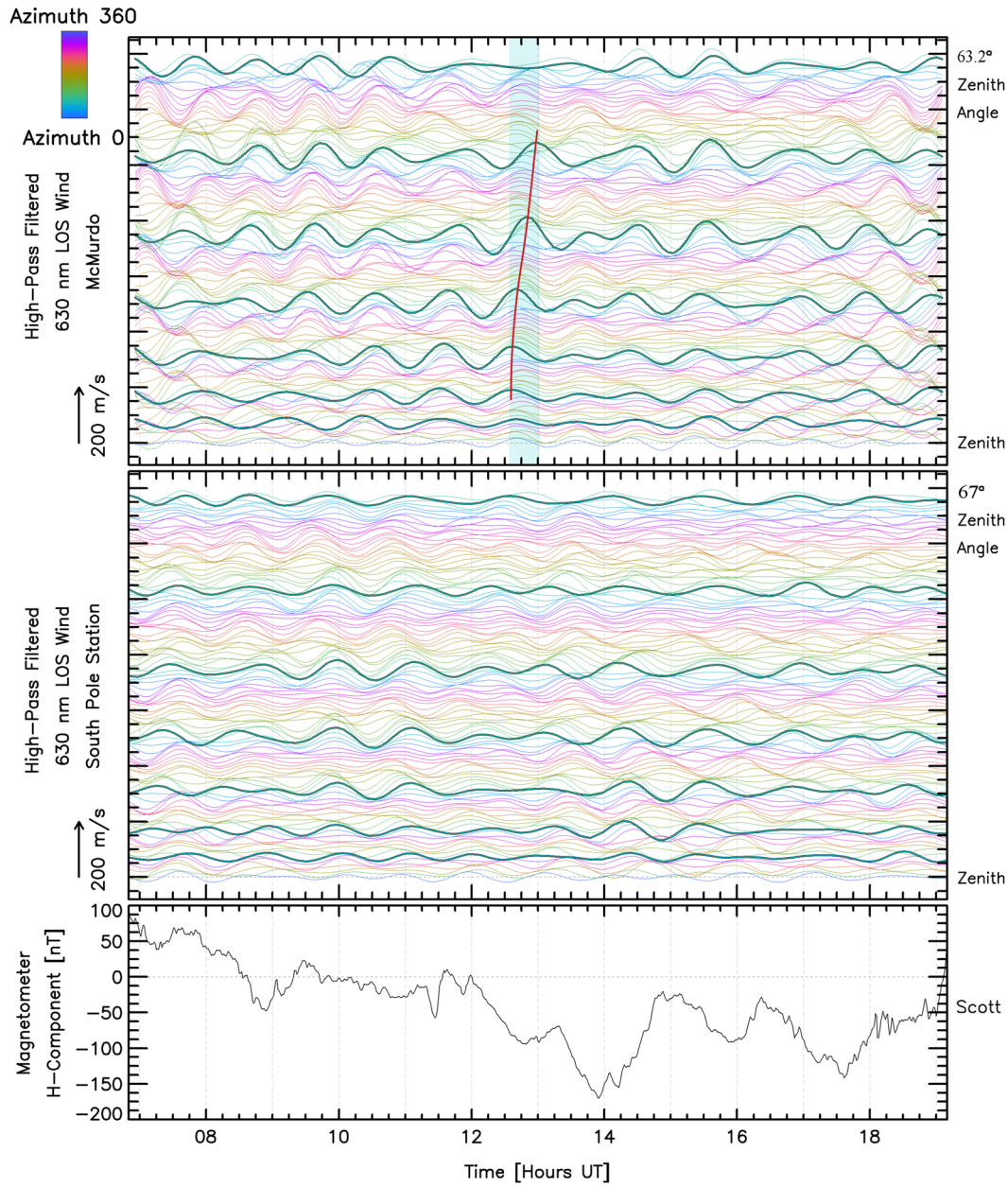

Figure 16. The top two panels show line-of-sight (LOS) wind oscillations as observed from McMurdo and South Pole Stations on 10 April 2018 (same day as in Figure 3) after applying a narrow band-pass filter that removed periods outside the range from 50 to 100 min. The reason for applying this rather restrictive pass band is to make the wave oscillations more readily discernible. As with Figure 3, green thicker traces highlight example azimuths from successive rings. In this case, azimuths near 160° are highlighted in the top panel and those near 200° in the middle panel. The red colored curve in the top panel between 12 and 13 UT connects example oscillation peaks from similar azimuths to emphasize the time lag between oscillations at different zenith angles. The bottom panel shows perturbations in the geomagnetic H-component recorded at Scott Base.

wind on the sine of the zenith angle. Although these values are for a single night, we only require a sanity check for the plausibility of interpreting the observed oscillations as wave signatures. These values are not intended to imply quantitative statistical moments of the wave field.

Inserting the observed estimates for u' and w' into Equation 4 shows that $k_z \simeq 3.8k_x$ for the waves observed here. This can then be substituted into the usual non-dissipative dispersion relation for thermospheric GWs (e.g., Vadas & Fritts, 2005)

$$\omega = \sqrt{\frac{k_x^2 \omega_b^2}{k_z^2 + k_x^2 + \left(\frac{1}{2H}\right)^2}} \tag{5}$$

and solved for k_x, from which the horizontal wavelength of these waves (using both lowest observed temporal period ≃60 min and the most dominant period ≃170 min observed in the F-region data) can be estimated to be

$$\lambda_x \simeq 39H \simeq 1750\,\text{km (for 60 min period)}, \tag{6}$$

and

$$\lambda_x \simeq 170H \simeq 7650\,\text{km (for 170 min period)}. \tag{7}$$

These values were obtained using estimates of $\omega_b \simeq 2\pi/(12\text{ min})$ and $H \simeq 45$ km—which are representative for conditions at F-region heights. The characteristic horizontal intrinsic phase speeds for the observed waves can then be estimated as:

$$v_{px} = \frac{\omega}{k_x} = \frac{2\pi/(60 * 60)\text{ s}}{2\pi/1750\text{ km}} \simeq 490\text{ m s}^{-1}\text{ (for 60 min period)}, \tag{8}$$

and

$$v_{px} = \frac{\omega}{k_x} = \frac{2\pi/(170 * 60)\text{ s}}{2\pi/7650\text{ km}} \simeq 750\text{ m s}^{-1}\text{ (for 170 min period)}. \tag{9}$$

The horizontal wavelength and horizontal phase speed calculated for 60 min period are well within the ranges previously observed for these parameters of thermospheric GWs at F-region heights (e.g., England et al., 2020; Miyoshi et al., 2018). Even though the observed wave period of 170 min is within the previously reported values, the corresponding horizontal wavelength appear very long compared to those reported previously.

Also, for a Brunt-Väisälä period of 12 min, and using the representative values encountered in this study of $\omega \sim 2\pi/(60\text{ min})$ and $\omega \sim 2\pi/(170\text{ min})$ and $w' \sim 9$ m/s, the right-hand side of Equation 3 predicts that the relative temperature perturbation $\left(T'/\overline{T}\right)$ due to the observed waves would be around 4% for 60 min period and 11% for 170 min period. These values of $T'/\overline{T}$ have a large uncertainty as the contributing factors have very high relative uncertainties—that is, 100% or more.

Finally, the predicted 90° phase shift between wind and temperature oscillations should provide a demanding test of whether the data are consistent with waves. Unfortunately, the observed waveforms were seldom monochromatic enough for this to be a definitive test. Figure 17 shows a small portion of the data, zoomed-in so that the phase relationship can be examined readily by making individual traces apparent. This shows that there was seldom, if ever, a simple phase relation between the observed wind and temperature oscillations. In particular, wind oscillations with a period of ∼60 min are easily discernible toward the top of the upper panel of Figure 17. However, the corresponding temperature oscillations are more difficult to discern.

It seems likely that the perturbations observed here are signatures of important processes in the thermospheric energy and momentum budgets. It is, therefore, crucial to understand the extent to which these perturbations are representative of traveling waves propagating in the real thermosphere. The next step would be to use the SDI data to investigate the distributions of phase speeds, horizontal wavelength, vertical wavelength, propagation directions, intrinsic periods, etc. Robust reconstruction of phase fronts would be facilitated by the multiple observing stations and look directions provided by the SDI instrument array. It would then be possible to infer the various wave parameters. However, this analysis would require fitting a two-dimensional field of traveling phase fronts to the data, which itself is a non-trivial forward modeling problem, even if there is just one simple monochromatic plane wave field present. If there are multiple wave packets, each with their own individual amplitudes, phase, propagation direction, period, etc., the analysis would become far more difficult.

As a final note, this study required manual inspection of hundreds of days of data from each site. Statistical metrics have not yet been developed to rigorously quantify the occurrence frequency of discernible wave activity. However, qualitatively, it was noticed that truly quiescent conditions were uncommon in the F-region above

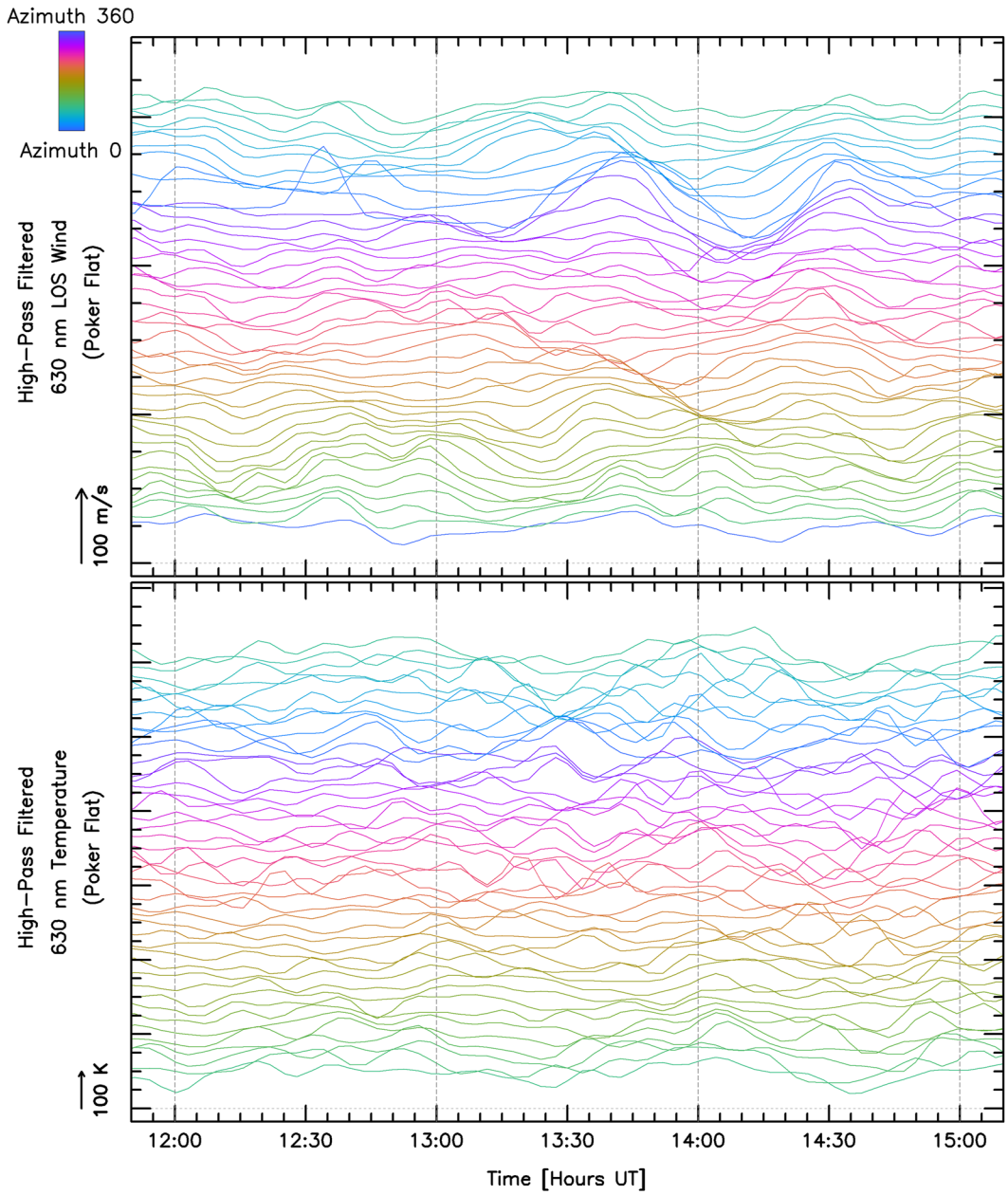

Figure 17. Zoomed-in subset of temperature and line-of-sight (LOS) wind oscillations observed on 7 November 2017, from Poker Flat, Alaska. This figure only shows 3 hr of data for selected zones (zones 217–260) in the outermost ring of the Scanning Doppler Imager field of view. These oscillations were generally complicated, such that it is difficult to discern any systematic phase relationship between wind and temperature oscillations.

most of the SDI sites. For all but one site, it was unusual to encounter a day when the instrument was functioning well, and the sky was clear, but the F-region wave signal was indistinguishable from noise. The one exception to this was the site at Mawson, for which the impression was formed that quiescent days were more common. To test this, approximately 130 clear nights of high-pass filtered 630 nm LOS wind data were examined. These observations were acquired from Mawson in 2011. We were unable to confidently recognize wave perturbations on roughly 40% of these days. By contrast, the unambiguous absence of waves was rare for all other sites. These results suggest that the wave field above Mawson can relax to a more quiescent state than it can elsewhere. One possible interpretation is that there is a background contribution of waves propagating up from the lower atmosphere that is seen by most sites apart from Mawson. This perhaps indicates that the orographic and/or meteorological generation of lower atmospheric waves is less significant at this site.

5. Conclusions

This study examined oscillatory perturbations in measurements of thermospheric temperature and wind derived from optical Doppler spectra. Significant oscillatory perturbations were unambiguously detected using high-pass temporal filtering. Their characteristics suggest that they are of geophysical origin. The objective of studying them was to examine the hypothesis that these perturbations could be signatures of GW activity. Perturbation amplitudes were observed to increase considerably during increased geophysical activity. While F-region wind perturbations were almost always detected at some level, the SDI instruments were less able to resolve oscillations in F-region temperatures or E-region winds. This is understood as arising because the perturbation amplitudes of F-region temperature and E-region winds are smaller relative to other sources of measurement variability and errors for these quantities. Nevertheless, the data do contain instances of apparent wavelike perturbations in those quantities as well.

The dependence of the perturbation amplitudes on geophysical activity, viewing zenith angle and viewing azimuth angle, and the strong coherence between oscillations in adjacent zones all indicate that the observed fluctuations were of geophysical origin rather than being due to measurement artifacts. Phase relations between the time series for the various viewing zones suggest that the observed perturbations were often consistent with expectations for a (typically complicated) field of traveling waves, although this was not always the case. Many instances of time-synchronous perturbations across all viewing zones were observed, that cannot be interpreted as signatures of waves.

Nevertheless, the data suggest that the technique can detect thermospheric GWs and, further, it shows that wave activity is common in Earth's thermosphere at auroral latitudes. Additionally, the data suggest that the wave response to the geomagnetic activity is similar in either hemisphere.

Azimuthal variation of phases throughout all of the data suggests that the wave field in the Earth's thermosphere is seldom a simple set of monochromatic plane phase fronts. Rather, it appears that the wave field is more typically composed of many different wave packets with widely varying amplitudes, phases, and propagation directions. Presumably, if such wave fields could be visualized, they would appear reminiscent of the complicated field of surface waves often seen on the ocean.

Sliding-window Lomb-Scargle analysis was performed on the LOS wind time series from selected nights to analyze how the spectrum of observed wave periods varied as a function of time during the night. The resulting periodograms showed that the wave spectra varied from zone to zone. Further, spectra also varied within individual zones over the course of a night. The shortest observed periods for F-region wind oscillations with statistically significant power were typically 60 min. By contrast, the spectrum of E-region waves extended to shorter periods—that is, as short as 30 min. Oscillations with periods up to 180 min were detected both at E- and F-region altitudes. Longer-period oscillations may occur, but those cannot be resolved with the current technique. Thermospheric GWs have been observed in previous studies over a broad range of periods extending from a few tens of minutes up to more than 12 hr (Ford et al., 2008; Katamzi-Joseph et al., 2019; Klausner et al., 2009; Richmond, 1978; Vadas & Fritts, 2006). The wave periods observed here fall well within this range. Observed E-region wind oscillations were often noisier and less monochromatic than the corresponding F-region wind perturbations, resulting in broader Lomb-Scargle spectra for E-region data. As discussed in Section 3.1.4, geophysical noise due to the altitude variation of the 558 nm emission layer could have contributed to this spectral broadening of the E-region time series. By contrast, the F-region LOS wind oscillations were relatively smooth, as expected.

The initial expectation was that oscillations observed during quiet geomagnetic conditions could be indications of disturbances propagating up from below, because in-situ wave generation would, presumably, be weak. Although wave perturbations likely do propagate up from the lower atmosphere, this study did not resolve such a component, because of the nearly ubiquitous background activity. More detailed analysis will be required to determine the relative contributions of in-situ forcing versus upward propagation.

There is more information in the SDI data than has been examined in this current work. Future studies will focus on phase lags and relative amplitudes of oscillations between time series recorded in different zones. Although relatively rare, it is expected that there would be some instances when the wave field is sufficiently simple that the relative amplitudes and phases between the zones could be used to infer the properties of at least the dominant

perturbations that are present. Measuring these phase lags would characterize properties such as the period, phase speed, and direction of phase propagation. This analysis would not be possible for observations made in a single look direction and would be less robust if only a small number of directions were viewed.

Data Availability Statement

Scanning Doppler Imager data are available at http://sdi_server.gi.alaska.edu/sdi_web_plots/. Solar radio flux density (F10.7) data were adopted from https://www.spaceweather.gc.ca/forecast-prevision/solar-solaire/solar-flux/sx-5-flux-en.php. Geomagnetic indices were taken from Geomagnetic Observatory Niemegk, GFZ German Research Center for Geosciences' website https://kp.gfz-potsdam.de/en/data#c39.

Acknowledgments
This research was supported by NSF award numbers 1341545 and 1452333. Magnetometer observations used in this work were provided by Geosciences Australia (Mawson), the New Zealand Antarctic Program (Scott Base), and the US Geological Survey (College), and accessed via the archive maintained by the International INTERMAGNET program (www.intermagnet.org). We also thank INTERMAGNET for promoting high standards of magnetic observatory practice.

References

Anderson, C., Conde, M., & McHarg, M. (2012). Neutral thermospheric dynamics observed with two scanning Doppler imagers: 3. Horizontal wind gradients. *Journal of Geophysical Research*, *117*, A05311. https://doi.org/10.1029/2011ja017471

Branning, K., Conde, M., Larsen, M., & Troyer, R. (2022). Resolving vertical variations of horizontal neutral winds in earth's high latitude space-atmosphere interaction region (SAIR). *Journal of Geophysical Research: Space Physics*, *127*(5), e2021JA029805. https://doi.org/10.1029/2021ja029805

Bruinsma, S. L., & Forbes, J. M. (2008). Medium-to large-scale density variability as observed by champ. *Space Weather*, *6*, S08002. https://doi.org/10.1029/2008sw000411

Conde, M. (2001). Analysis of Fabry-Perot spectra of lidar backscatter echoes. *ANARE Reports*, *146*, 91–114.

Conde, M., Bristow, W., Hampton, D., & Elliott, J. (2018). Multiinstrument studies of thermospheric weather above Alaska. *Journal of Geophysical Research: Space Physics*, *123*(11), 9836–9861. https://doi.org/10.1029/2018ja025806

Conde, M., Craven, J., Immel, T., Hoch, E., Stenbaek-Nielsen, H., Hallinan, T., et al. (2001). Assimilated observations of thermospheric winds, the aurora, and ionospheric currents over Alaska. *Journal of Geophysical Research*, *106*(A6), 10493–10508. https://doi.org/10.1029/2000ja000135

Conde, M., & Smith, R. (1998). Spatial structure in the thermospheric horizontal wind above poker flat, Alaska, during solar minimum. *Journal of Geophysical Research*, *103*(A5), 9449–9471. https://doi.org/10.1029/97ja03331

Djuth, F., Sulzer, M., Elder, J., & Wickwar, V. (1997). High-resolution studies of atmosphere-ionosphere coupling at Arecibo Observatory, Puerto Rico. *Radio Science*, *32*(6), 2321–2344. https://doi.org/10.1029/97rs02797

Djuth, F., Sulzer, M., Gonzales, S., Mathews, J., Elder, J., & Walterscheid, R. (2004). A continuum of gravity waves in the Arecibo thermosphere? *Geophysical Research Letters*, *31*(16), L16801. https://doi.org/10.1029/2003gl019376

England, S. L., Greer, K. R., Solomon, S. C., Eastes, R. W., McClintock, W. E., & Burns, A. G. (2020). Observation of thermospheric gravity waves in the Southern Hemisphere with gold. *Journal of Geophysical Research: Space Physics*, *125*(4), e2019JA027405. https://doi.org/10.1029/2019ja027405

Ford, E., Aruliah, A., Griffin, E., & McWhirter, I. (2008). Statistical analysis of thermospheric gravity waves from Fabry-Perot interferometer measurements of atomic oxygen. *Annales Geophysicae*, *26*(1), 29–45. https://doi.org/10.5194/angeo-26-29-2008

Fritts, D. C., & Alexander, M. J. (2003). Gravity wave dynamics and effects in the middle atmosphere. *Reviews of Geophysics*, *41*, 1003. https://doi.org/10.1029/2001rg000106

Fukushima, D., Shiokawa, K., Otsuka, Y., & Ogawa, T. (2012). Observation of equatorial nighttime medium-scale traveling ionospheric disturbances in 630-nm airglow images over 7 years. *Journal of Geophysical Research*, *117*, A10324. https://doi.org/10.1029/2012ja017758

Gabrielse, C., Nishimura, T., Chen, M., Hecht, J. H., Kaeppler, S. R., Gillies, D. M., et al. (2021). Estimating precipitating energy flux, average energy, and hall auroral conductance from THEMIS all-sky-imagers with focus on mesoscales. *Frontiers in Physics*, *9*, 744298. https://doi.org/10.3389/fphy.2021.744298

Galvan, D. A., Komjathy, A., Hickey, M. P., & Mannucci, A. J. (2011). The 2009 Samoa and 2010 Chile tsunamis as observed in the ionosphere using GPS total electron content. *Journal of Geophysical Research*, *116*, A06318. https://doi.org/10.1029/2010ja016204

Garcia, R. F., Bruinsma, S., Massarweh, L., & Doornbos, E. (2016). Medium-scale gravity wave activity in the thermosphere inferred from GOCE data. *Journal of Geophysical Research: Space Physics*, *121*(8), 8089–8102. https://doi.org/10.1002/2016ja022797

Hays, P., Nagy, A. F., & Roble, R. (1969). Interferometric measurements of the 6300 a Doppler temperature during a magnetic storm. *Journal of Geophysical Research*, *74*(16), 4162–4168. https://doi.org/10.1029/ja074i016p04162

Hecht, J., Strickland, D., & Conde, M. (2006). The application of ground-based optical techniques for inferring electron energy deposition and composition change during auroral precipitation events. *Journal of Atmospheric and Solar-Terrestrial Physics*, *68*(13), 1502–1519. https://doi.org/10.1016/j.jastp.2005.06.022

Hernandez, G. (1982). Vertical motions of the neutral thermosphere at midlatitude. *Geophysical Research Letters*, *9*(5), 555–557. https://doi.org/10.1029/gl009i005p00555

Hickey, M., Schubert, G., & Walterscheid, R. (2010). Atmospheric airglow fluctuations due to a tsunami-driven gravity wave disturbance. *Journal of Geophysical Research*, *115*, A06308. https://doi.org/10.1029/2009ja014977

Hines, C. O. (1960). Internal atmospheric gravity waves at ionospheric heights. *Canadian Journal of Physics*, *38*(11), 1441–1481. https://doi.org/10.1139/p60-150

Hocke, K., & Schlegel, K. (1996). A review of atmospheric gravity waves and travelling ionospheric disturbances: 1982–1995. *Annales Geophysicae*, *14*(9), 917–940. https://doi.org/10.1007/s00585-996-0917-6

Innis, J. (2000). Deceleration of the high-latitude thermospheric wind by polar cap gravity waves. *Geophysical Research Letters*, *27*(23), 3813–3816. https://doi.org/10.1029/2000gl012066

Innis, J., Greet, P., & Dyson, P. (1996). Fabry-Perot spectrometer observations of the auroral oval/polar cap boundary above Mawson, Antarctica. *Journal of Atmospheric and Terrestrial Physics*, *58*(16), 1973–1988. https://doi.org/10.1016/0021-9169(96)00007-4

Itani, R., & Conde, M. (2021). Characterizing unexpectedly localized slowing of the thermospheric cross-polar jet of neutral wind over Alaska in the midnight sector. *Journal of Geophysical Research: Space Physics*, *126*(10), e2020JA028916. https://doi.org/10.1029/2020ja028916

Johnson, F., Hanson, W., Hodges, R., Coley, W., Carignan, G., & Spencer, N. (1995). Gravity waves near 300 km over the polar caps. *Journal of Geophysical Research*, *100*(A12), 23993–24002. https://doi.org/10.1029/95ja02858

Kaeppler, S., Hampton, D., Nicolls, M., Strømme, A., Solomon, S., Hecht, J., & Conde, M. (2015). An investigation comparing ground-based techniques that quantify auroral electron flux and conductance. *Journal of Geophysical Research: Space Physics*, *120*(10), 9038–9056. https://doi.org/10.1002/2015ja021396

Katamzi-Joseph, Z. T., Aruliah, A. L., Oksavik, K., Habarulema, J. B., Kauristie, K., & Kosch, M. J. (2019). Multi-instrument observations of large-scale atmospheric gravity waves/traveling ionospheric disturbances associated with enhanced auroral activity over Svalbard. *Advances in Space Research*, *63*(1), 270–281. https://doi.org/10.1016/j.asr.2018.08.042

Killeen, T., Craven, J., Frank, L., Ponthieu, J.-J., Spencer, N., Heelis, R., et al. (1988). On the relationship between dynamics of the polar thermosphere and morphology of the aurora: Global-scale observations from dynamics explorers 1 and 2. *Journal of Geophysical Research*, *93*(A4), 2675–2692. https://doi.org/10.1029/ja093ia04p02675

Killeen, T., & Roble, R. (1988). Thermosphere dynamics: Contributions from the first 5 years of the dynamics explorer program. *Reviews of Geophysics*, *26*(2), 329–367. https://doi.org/10.1029/rg026i002p00329

Klausner, V., Fagundes, P., Sahai, Y., Wrasse, C., Pillat, V., & Becker-Guedes, F. (2009). Observations of GW/TID oscillations in the *F*2 layer at low latitude during high and low solar activity, geomagnetic quiet and disturbed periods. *Journal of Geophysical Research*, *114*, A02313. https://doi.org/10.1029/2008ja013448

Larsen, M. (2002). Winds and shears in the mesosphere and lower thermosphere: Results from four decades of chemical release wind measurements. *Journal of Geophysical Research*, *107*(A8), SIA28-1–SIA28-14. https://doi.org/10.1029/2001ja000218

Lomb, N. R. (1976). Least-squares frequency analysis of unequally spaced data. *Astrophysics and Space Science*, *39*(2), 447–462. https://doi.org/10.1007/bf00648343

McCormac, F., Killeen, T. L., Nardi, B., & Smith, R. (1987). How close are ground-based Fabry-Perot thermospheric wind and temperature measurements to exospheric values? A simulation study. *Planetary and Space Science*, *35*(10), 1255–1265. https://doi.org/10.1016/0032-0633(87)90110-3

Miyoshi, Y., Jin, H., Fujiwara, H., & Shinagawa, H. (2018). Numerical study of traveling ionospheric disturbances generated by an upward propagating gravity wave. *Journal of Geophysical Research: Space Physics*, *123*(3), 2141–2155. https://doi.org/10.1002/2017ja025110

Nicolls, M., Vadas, S., Meriwether, J., Conde, M., & Hampton, D. (2012). The phases and amplitudes of gravity waves propagating and dissipating in the thermosphere: Application to measurements over Alaska. *Journal of Geophysical Research*, *117*, A05323. https://doi.org/10.1029/2012ja017542

Oliver, W., Otsuka, Y., Sato, M., Takami, T., & Fukao, S. (1997). A climatology of *F* region gravity wave propagation over the middle and upper atmosphere radar. *Journal of Geophysical Research*, *102*(A7), 14499–14512. https://doi.org/10.1029/97ja00491

Oyama, S., Ishii, M., Murayama, Y., Shinagawa, H., Buchert, S., Fujii, R., & Kofman, W. (2001). Generation of atmospheric gravity waves associated with auroral activity in the polar *F* region. *Journal of Geophysical Research*, *106*(A9), 18543–18554. https://doi.org/10.1029/2001ja900032

Paulino, I., Medeiros, A., Vadas, S., Wrasse, C., Takahashi, H., Buriti, R., et al. (2016). Periodic waves in the lower thermosphere observed by OI630 nm airglow images. *Annales Geophysicae*, *34*(2), 293–301. https://doi.org/10.5194/angeo-34-293-2016

Richmond, A. (1978). Gravity wave generation, propagation, and dissipation in the thermosphere. *Journal of Geophysical Research*, *83*(A9), 4131–4145. https://doi.org/10.1029/ja083ia09p04131

Scargle, J. D. (1982). Studies in astronomical time series analysis. II-Statistical aspects of spectral analysis of unevenly spaced data. *The Astrophysical Journal*, *263*, 835–853. https://doi.org/10.1086/160554

Sica, R., Rees, M., Roble, R. G., Hernandez, G., & Romick, G. (1986). The altitude region sampled by ground-based Doppler temperature measurements of the OI 15867 K emission line in aurorae. *Planetary and Space Science*, *34*(5), 483–488. https://doi.org/10.1016/0032-0633(86)90035-8

Smith, S., Vadas, S., Baggaley, W., Hernandez, G., & Baumgardner, J. (2013). Gravity wave coupling between the mesosphere and thermosphere over New Zealand. *Journal of Geophysical Research: Space Physics*, *118*(5), 2694–2707. https://doi.org/10.1002/jgra.50263

Vadas, S. L., & Azeem, I. (2020). Concentric secondary gravity waves in the thermosphere and ionosphere over the continental United States on 25-26 march 2015 from deep convection. *Journal of Geophysical Research: Space Physics*, *126*(2), e2020JA028275. https://doi.org/10.1029/2020JA028275

Vadas, S. L., & Fritts, D. C. (2005). Thermospheric responses to gravity waves: Influences of increasing viscosity and thermal diffusivity. *Journal of Geophysical Research*, *110*(D15), D15103. https://doi.org/10.1029/2004jd005574

Vadas, S. L., & Fritts, D. C. (2006). Influence of solar variability on gravity wave structure and dissipation in the thermosphere from tropospheric convection. *Journal of Geophysical Research*, *111*(A10), A10S12. https://doi.org/10.1029/2005ja011510

Vadas, S. L., & Liu, H.-L. (2009). Generation of large-scale gravity waves and neutral winds in the thermosphere from the dissipation of convectively generated gravity waves. *Journal of Geophysical Research*, *114*, A10310. https://doi.org/10.1029/2009ja014108

Vadas, S. L., Zhao, J., Chu, X., & Becker, E. (2018). The excitation of secondary gravity waves from local body forces: Theory and observation. *Journal of Geophysical Research: Atmospheres*, *123*(17), 9296–9325. https://doi.org/10.1029/2017jd027970

Yeh, K. C., & Liu, C. H. (1974). Acoustic-gravity waves in the upper atmosphere. *Reviews of Geophysics*, *12*(2), 193–216. https://doi.org/10.1029/rg012i002p00193

Yiğit, E., & Medvedev, A. S. (2012). Gravity waves in the thermosphere during a sudden stratospheric warming. *Geophysical Research Letters*, *39*, L21101. https://doi.org/10.1029/2012gl053812

Yiğit, E., & Medvedev, A. S. (2019). Obscure waves in planetary atmospheres: On earth and on other planets, internal gravity waves shape the dynamics and thermodynamics of the atmosphere. *Physics Today*, *72*(6), 40–46. https://doi.org/10.1063/pt.3.4226

Yu, Y. (2007). *Model studies of time-dependent ducting for high-frequency gravity waves and associated airglow responses in the upper atmosphere*. University of Central Florida.